

A systematic study of lepton flavor violating dark matter interactions via indirect detection in effective field theories

Sahabub Jahedi ,^{1,2} Jin-Han Liang ,^{1,2,*} Yi Liao ,^{1,2,†} Xiao-Dong Ma ,^{1,2,‡} and Yoshiki Uchida ,^{1,2}

¹*State Key Laboratory of Nuclear Physics and Technology, Institute of Quantum Matter,
South China Normal University, Guangzhou 510006, China*

²*Guangdong Basic Research Center of Excellence for Structure and Fundamental Interactions of Matter,
Guangdong Provincial Key Laboratory of Nuclear Science, Guangzhou 510006, China*

Lepton flavor violating (LFV) interactions involving dark matter (DM) particles remain a largely unexplored area. In this study, we systematically investigate LFV DM interactions within the framework of effective field theories by analyzing astrophysical photons and positrons produced from DM annihilation. Employing the astrophysical photon and positron data collected by Fermi-LAT, INTEGRAL, XMM-Newton, and AMS-02, we place meaningful constraints on all leading-order effective operators involving a DM pair and a flavor violating charged lepton pair. Our analysis covers the three well-known DM candidates: a scalar, a fermion, and a vector particle. For the photon flux, we consider contributions from final-state radiation, radiative decay, and inverse Compton scattering, and examine their respective sensitivity regions across different DM masses and photon energies. We find that for DM masses below $\mathcal{O}(20\text{ GeV})$, INTEGRAL provides the most stringent constraints on annihilation cross sections and effective operators in all three LFV channels, whereas AMS-02 offers the strongest constraints above $\mathcal{O}(20\text{ GeV})$.

I. INTRODUCTION

The existence of dark matter (DM) is strongly supported by astrophysical observations. However, despite decades of theoretical and experimental studies, its microscopic nature remains elusive. Among various DM scenarios, the \mathbb{Z}_2 -symmetry-protected DM candidate represents a compelling possibility that naturally ensures its longevity on cosmological timescales. Over the years, this type of DM candidate has been extensively studied experimentally through direct and indirect detection methods, as well as via direct production at colliders. Although no positive signals have been observed so far, stringent upper limits have been established on the relevant observables and couplings [1–8]. A key assumption underlying these searches is that the DM pairs couple to pairs of standard model (SM) particles in a flavor-conserving manner.

Given the stringent limits on flavor-conserving DM interactions and our limited understanding of its true nature, extending the investigation of DM-SM interactions into the flavor-violating sector may offer valuable new insights. Flavor-changing neutral current (FCNC) DM-quark interactions serve as an illuminating example, as they could potentially connect DM to flavor anomalies such as the $B \rightarrow K\nu\bar{\nu}$ excess reported in Belle II measurements [9–15]. In contrast, lepton-flavor-violating (LFV) DM interactions remain largely unexplored. Such interactions are common in various new physics (NP) models, including scotogenic seesaw scenarios that simultaneously address neutrino masses and DM candidates [16, 17], lepton-flavored DM models [18], the axion-

or ALP-mediated frameworks [19], and others. Given the variety of model frameworks, it is worthwhile to systematically study such interactions from the perspective of effective field theories (EFT), making minimal assumptions about the underlying dynamics.

EFT is a tailored tool for studying low-energy processes with small momentum transfer, such as those relevant to DM direct and indirect detections. In the low-energy EFT extended with an additional DM particle, known as dark sector EFT (DSEFT) [20, 21], the LFV DM-charged lepton interactions take a factorized form, $DM^2 \ell_i \Gamma \ell_{j \neq i}$, where the lepton flavor indices $i, j = e, \mu, \tau$. Recently, we initiated a study of these interactions by examining the LFV decays of the μ and τ leptons involving a pair of light DM in the final state [22], focusing on the DM mass range $m_{\text{DM}} \lesssim |m_i - m_j|/2$. Beyond this mass threshold, indirect detection of DM becomes a valuable approach to probe the relevant parameter space [23]. In the present work, we aim to extend this investigation to probe the heavier DM mass range by analyzing indirect detection signals of DM annihilation, including photons and positrons, as observed by Fermi-LAT [24], INTEGRAL [25], XMM-Newton [26], and AMS-02 [27].

In this analysis, we consider three well-known DM candidates with spin up to 1, including a spin-0 scalar DM ϕ (either complex or real), a spin-1/2 fermion DM χ (either Dirac or Majorana), and a spin-1 vector DM X (either complex or real). For each case, we identify the leading-order effective operators and study constraints on their Wilson coefficients (WCs) from indirect detection signatures. We calculate the photon flux induced by various mechanisms, including prompt photons from final state radiation (FSR) and radiative decays (Rad) of charged leptons, and non-prompt photons from inverse Compton scattering of electrons or positrons off the background photons. In particular, we will demonstrate that the normalized FSR photon spectra from all s-wave operators in

* jinhanliang@m.scnu.edu.cn

† liaoy@m.scnu.edu.cn

‡ maxid@scnu.edu.cn

each specific annihilation channel exhibit a nearly degenerate pattern.

For the two-to-two annihilation processes $\text{DM} + \text{DM} \rightarrow \ell_i^\mp \ell_j^\pm$, these operators exhibit rich partial wave contributions, including both s-, p-, and d-waves. We find that 20 operators induce DM annihilation via the s-wave at leading order, while 12 operators lead to the p-wave annihilation. In addition, in the fermion DM case, two operators $\mathcal{O}_{\ell X 2}^{\text{V(A)}}$ involve both s- and p-wave contributions at leading order, whereas in the vector DM case, two operators $\mathcal{O}_{\ell X 3}^{\text{V(A)}}$ involve both p- and d-wave contributions. Unlike the common assumption of s-wave dominance, the p- and d-wave contributions are highly sensitive to the DM velocity distribution and generally lead to weaker constraints on the relevant annihilation cross sections and EFT WCs. Our results indicate that the constraints on effective scales associated with p-wave operators are weaker by one to two orders of magnitude compared to those on s-wave operators of the same dimension. For the dimension-6 (dim-6) operators in the fermion DM scenario, the effective scale can be probed from a few tens of GeV to TeV range for the s-wave operators, with the exact constraints varying according to the DM masses. These results complement existing constraints from charged LFV decays for DM masses below the annihilation thresholds.

The remainder of this paper is organized as follows. In Section II, we present all leading-order operators involving a DM pair and a LFV charged lepton current, and derive DM annihilation cross sections and their velocity expansions. The calculation of photon and positron fluxes arising from various mechanisms is detailed in Section III. The datasets used in our analysis, together with our final constraints on thermally averaged cross sections and EFT operators are presented in Section IV. Finally, our summary is offered in Section V. Section A provides a concise derivation of the thermally averaged cross section for a general velocity-dependent annihilation scenario.

II. LFV DM ANNIHILATION IN DSEFT

A. Effective lepton-DM operators in DSEFT

We work in the DSEFT framework and focus on the leading-order effective operators involving a pair of DM particles and a pair of charged leptons with distinct flavors [20, 21]. The relevant operators respecting the unbroken SM gauge symmetry $\text{SU}(3)_c \otimes \text{U}(1)_{\text{em}}$ are summarized in Table I, where the SM charged lepton fields are denoted by $\ell_{i,j} = e, \mu, \tau$. For the vector DM, we follow Ref. [20] and consider two parameterizations depending on whether the vector field is represented by a four-vector potential X_μ (case A) or a field strength tensor $X_{\mu\nu} \equiv \partial_\mu X_\nu - \partial_\nu X_\mu$ (case B). In vector DM case A, the covariant derivative for the operator $\mathcal{O}_{\ell X 1}^{\text{V}}$ is defined as $\bar{\ell}_i \gamma_{(\mu} i \overleftrightarrow{D}_\nu \ell_j \equiv i(\bar{\ell}_i \gamma_\mu D_\nu \ell_j - \bar{D}_\nu \ell_i \gamma_\mu \ell_j) + \mu \leftrightarrow \nu$,

| Scalar DM case | |
|--|---|
| $\mathcal{O}_{\ell \phi}^{\text{S},ij} = (\bar{\ell}_i \ell_j)(\phi^\dagger \phi)$ | $\mathcal{O}_{\ell \phi}^{\text{P},ij} = (\bar{\ell}_i i \gamma_5 \ell_j)(\phi^\dagger \phi)$ |
| $\mathcal{O}_{\ell \phi}^{\text{A},ij} = (\bar{\ell}_i \gamma^\mu \ell_j)(\phi^\dagger i \overleftrightarrow{D}_\mu \phi)(\mathbf{x})$ | $\mathcal{O}_{\ell \phi}^{\text{A},ij} = (\bar{\ell}_i \gamma^\mu \gamma_5 \ell_j)(\phi^\dagger i \overleftrightarrow{D}_\mu \phi)(\mathbf{x})$ |
| Fermion DM case | |
| $\mathcal{O}_{\ell \chi}^{\text{S},ij} = (\bar{\ell}_i \ell_j)(\bar{\chi} \chi)$ | $\mathcal{O}_{\ell \chi}^{\text{P},ij} = (\bar{\ell}_i i \gamma_5 \ell_j)(\bar{\chi} \chi)$ |
| $\mathcal{O}_{\ell \chi}^{\text{S},ij} = (\bar{\ell}_i \ell_j)(\bar{\chi} i \gamma_5 \chi)$ | $\mathcal{O}_{\ell \chi}^{\text{P},ij} = (\bar{\ell}_i \gamma_5 \ell_j)(\bar{\chi} \gamma_5 \chi)$ |
| $\mathcal{O}_{\ell \chi}^{\text{V},ij} = (\bar{\ell}_i \gamma^\mu \ell_j)(\bar{\chi} \gamma_\mu \chi)$ | $\mathcal{O}_{\ell \chi}^{\text{A},ij} = (\bar{\ell}_i \gamma^\mu \gamma_5 \ell_j)(\bar{\chi} \gamma_\mu \chi)$ |
| $\mathcal{O}_{\ell \chi}^{\text{V},ij} = (\bar{\ell}_i \gamma^\mu \ell_j)(\bar{\chi} \gamma_\mu \gamma_5 \chi)$ | $\mathcal{O}_{\ell \chi}^{\text{A},ij} = (\bar{\ell}_i \gamma^\mu \gamma_5 \ell_j)(\bar{\chi} \gamma_\mu \gamma_5 \chi)$ |
| $\mathcal{O}_{\ell \chi}^{\text{T},ij} = (\bar{\ell}_i \sigma^{\mu\nu} \ell_j)(\bar{\chi} \sigma_{\mu\nu} \chi)$ | $\mathcal{O}_{\ell \chi}^{\text{T},ij} = (\bar{\ell}_i \sigma^{\mu\nu} \ell_j)(\bar{\chi} \sigma_{\mu\nu} \gamma_5 \chi)$ |
| Vector DM case A | |
| $\mathcal{O}_{\ell X}^{\text{S},ij} = (\bar{\ell}_i \ell_j)(X_\mu^\dagger X^\mu)$ | $\mathcal{O}_{\ell X}^{\text{P},ij} = (\bar{\ell}_i i \gamma_5 \ell_j)(X_\mu^\dagger X^\mu)$ |
| $\mathcal{O}_{\ell X}^{\text{T},ij} = \frac{i}{2}(\bar{\ell}_i \sigma^{\mu\nu} \ell_j)(X_\mu^\dagger X_\nu - X_\nu^\dagger X_\mu)(\mathbf{x})$ | $\mathcal{O}_{\ell X}^{\text{T},ij} = \frac{1}{2}(\bar{\ell}_i \sigma^{\mu\nu} \gamma_5 \ell_j)(X_\mu^\dagger X_\nu - X_\nu^\dagger X_\mu)(\mathbf{x})$ |
| $\mathcal{O}_{\ell X}^{\text{V},ij} = \frac{1}{2}(\bar{\ell}_i \gamma_{(\mu} i \overleftrightarrow{D}_{\nu)})(X_\mu^\dagger X_\nu + X_\nu^\dagger X_\mu)$ | $\mathcal{O}_{\ell X}^{\text{A},ij} = \frac{1}{2}(\bar{\ell}_i \gamma_{(\mu} \gamma_5 i \overleftrightarrow{D}_{\nu)} \ell_j)(X_\mu^\dagger X_\nu + X_\nu^\dagger X_\mu)$ |
| $\mathcal{O}_{\ell X}^{\text{V},ij} = (\bar{\ell}_i \gamma_\mu \ell_j) \partial_\nu (X_\mu^\dagger X_\nu + X_\nu^\dagger X_\mu)$ | $\mathcal{O}_{\ell X}^{\text{A},ij} = (\bar{\ell}_i \gamma_\mu \gamma_5 \ell_j) \partial_\nu (X_\mu^\dagger X_\nu + X_\nu^\dagger X_\mu)$ |
| $\mathcal{O}_{\ell X}^{\text{V},ij} = (\bar{\ell}_i \gamma_\mu \ell_j) (X_\mu^\dagger \overleftrightarrow{D}_\nu X_\sigma) \epsilon^{\mu\nu\rho\sigma}$ | $\mathcal{O}_{\ell X}^{\text{A},ij} = (\bar{\ell}_i \gamma_\mu \gamma_5 \ell_j) (X_\mu^\dagger \overleftrightarrow{D}_\nu X_\sigma) \epsilon^{\mu\nu\rho\sigma}$ |
| $\mathcal{O}_{\ell X}^{\text{V},ij} = (\bar{\ell}_i \gamma_\mu \ell_j) i \partial_\nu (X_\mu^\dagger X_\nu - X_\nu^\dagger X_\mu)(\mathbf{x})$ | $\mathcal{O}_{\ell X}^{\text{A},ij} = (\bar{\ell}_i \gamma_\mu \gamma_5 \ell_j) i \partial_\nu (X_\mu^\dagger X_\nu - X_\nu^\dagger X_\mu)(\mathbf{x})$ |
| $\mathcal{O}_{\ell X}^{\text{V},ij} = (\bar{\ell}_i \gamma_\mu \ell_j) i \partial_\nu (X_\mu^\dagger X_\sigma) \epsilon^{\mu\nu\rho\sigma}(\mathbf{x})$ | $\mathcal{O}_{\ell X}^{\text{A},ij} = (\bar{\ell}_i \gamma_\mu \gamma_5 \ell_j) i \partial_\nu (X_\mu^\dagger X_\sigma) \epsilon^{\mu\nu\rho\sigma}(\mathbf{x})$ |
| Vector DM case B | |
| $\tilde{\mathcal{O}}_{\ell X 1}^{\text{S},ij} = (\bar{\ell}_i \ell_j) X_{\mu\nu}^\dagger X^{\mu\nu}$ | $\tilde{\mathcal{O}}_{\ell X 2}^{\text{S},ij} = (\bar{\ell}_i \ell_j) X_{\mu\nu}^\dagger \tilde{X}^{\mu\nu}$ |
| $\tilde{\mathcal{O}}_{\ell X 1}^{\text{P},ij} = (\bar{\ell}_i i \gamma_5 \ell_j) X_{\mu\nu}^\dagger X^{\mu\nu}$ | $\tilde{\mathcal{O}}_{\ell X 2}^{\text{P},ij} = (\bar{\ell}_i i \gamma_5 \ell_j) X_{\mu\nu}^\dagger \tilde{X}^{\mu\nu}$ |
| $\tilde{\mathcal{O}}_{\ell X 1}^{\text{T},ij} = \frac{i}{2}(\bar{\ell}_i \sigma^{\mu\nu} \ell_j)(X_{\mu\nu}^\dagger X_\rho^\mu - X_\rho^\dagger X_{\mu\nu})(\mathbf{x})$ | $\tilde{\mathcal{O}}_{\ell X 2}^{\text{T},ij} = \frac{1}{2}(\bar{\ell}_i \sigma^{\mu\nu} \gamma_5 \ell_j)(X_{\mu\nu}^\dagger X_\rho^\mu - X_\rho^\dagger X_{\mu\nu})(\mathbf{x})$ |

TABLE I. The leading-order effective operators containing a lepton bilinear and a pair of DM particles in the DSEFT framework [20]. Here, the flavor indices $ij = e\mu(\mu e), e\tau(\tau e), \mu\tau(\tau\mu)$.

and similarly for the operator $\mathcal{O}_{\ell X 1}^{\text{A}}$ by replacing γ_μ with $\gamma_\mu \gamma_5$. In vector DM case B, the dual field strength tensor is given by $\tilde{X}^{\mu\nu} = (1/2)\epsilon^{\mu\nu\rho\sigma} X_{\rho\sigma}$. In the table, the ‘ \mathbf{x} ’ symbol indicates that the relevant operator vanishes when the DM particle is its own antiparticle.

According to the effective operators listed in Table I, it is straightforward to calculate the DM annihilation cross section in each case and its corresponding partial-wave expansion in terms of the DM relative velocity v_{rel} . For our analysis, the relevant annihilation channels are two-to-two processes $\text{DM} + \text{DM} \rightarrow \ell_i^- \ell_j^+$. Their thermally averaged annihilation cross sections $\langle \sigma v_{\text{rel}} \rangle_{ij}$ directly determine the predicted photon and positron fluxes, which will be detailed in the next section. Consequently, to derive constraints on the WCs from existing astrophysical observations, it is necessary to calculate the annihilation cross sections, as we discuss in the following subsection.

B. Calculation of annihilation cross sections

The total annihilation cross section of a specific process $\text{DM}(k_1) + \text{DM}(k_2) \rightarrow \ell_i^-(p_i) \ell_j^+(p_j)$ is expressed as

$$\sigma = \frac{1}{16\pi\lambda(s, m_{\text{DM}}^2, m_{\text{DM}}^2)} \int_{\frac{1}{2}(t_+ - t_-)}^{\frac{1}{2}(t_+ + t_-)} \overline{|\mathcal{M}|^2} dt, \quad (1)$$

where $\overline{|\mathcal{M}|^2}$ denotes the spin-averaged and -summed matrix element squared. $s \equiv (k_1 + k_2)^2$ is the invariant mass squared of the DM pair, and $t \equiv (k_1 - p_i)^2$ with

$$t_- = \frac{1}{s} \sqrt{\lambda(s, m_{\text{DM}}^2, m_{\text{DM}}^2) \lambda(s, m_i^2, m_j^2)}, \quad (2a)$$

| Operator | Total cross section $\sigma [C_i^j ^2]$ | Leading-order $\sigma v_{\text{rel}} [C_i^j ^2]$ |
|--|--|--|
| Scalar DM case | | |
| $\mathcal{O}_{\ell\phi}^{\text{S},ij}(\mathcal{O}_{\ell\phi}^{\text{P},ij})$ | $\frac{\sqrt{\rho+\rho_-}}{8\pi s^2\sqrt{\kappa_f}}\rho_-$, | $\frac{1}{4\pi}(1-\eta_{ij})^2$. |
| $\mathcal{O}_{\ell\phi}^{\text{V},ij}(\mathcal{O}_{\ell\phi}^{\text{A},ij})$ | $\frac{\sqrt{\kappa_f\rho+\rho_-}}{24\pi s^2}\rho_+(3s-\rho_-)$, | $\frac{m_\phi^2}{12\pi}(1-\eta_{ij})^2(2+\eta_{ij})v_{\text{rel}}^2$. |
| Fermion DM case | | |
| $\mathcal{O}_{\ell\chi 1}^{\text{S},ij}(\mathcal{O}_{\ell\chi 1}^{\text{P},ij})$ | $\frac{\sqrt{\kappa_f\rho+\rho_-}}{16\pi s}\rho_-$, | $\frac{m_\chi^2}{8\pi}(1-\eta_{ij})^2v_{\text{rel}}^2$. |
| $\mathcal{O}_{\ell\chi 2}^{\text{S},ij}(\mathcal{O}_{\ell\chi 2}^{\text{P},ij})$ | $\frac{\sqrt{\rho+\rho_-}}{16\pi s\sqrt{\kappa_f}}\rho_-$, | $\frac{m_\chi^2}{2\pi}(1-\eta_{ij})^2$. |
| $\mathcal{O}_{\ell\chi 1}^{\text{V},ij}(\mathcal{O}_{\ell\chi 1}^{\text{A},ij})$ | $\frac{\sqrt{\rho+\rho_-}}{48\pi s^2\sqrt{\kappa_f}}(3-\kappa_f)\rho_+(3s-\rho_-)$, | $\frac{m_\chi^2}{2\pi}(1-\eta_{ij})^2(2+\eta_{ij})$. |
| $\mathcal{O}_{\ell\chi 2}^{\text{V},ij}(\mathcal{O}_{\ell\chi 2}^{\text{A},ij})$ | $\frac{\sqrt{\rho+\rho_-}}{48\pi s^2\sqrt{\kappa_f}}\{3s[2\kappa_f\rho_+ + (1-\kappa_f)\rho_-] - (3-\kappa_f)\rho_+\rho_-\}$, | $\frac{m_\chi^2}{2\pi}\eta_{ij}(1-\eta_{ij})^2$ $+ \frac{m_\chi^2}{24\pi}(1-\eta_{ij})(4-5\eta_{ij}+7\eta_{ij}^2)v_{\text{rel}}^2$. |
| $\mathcal{O}_{\ell\chi 1}^{\text{T},ij}(\mathcal{O}_{\ell\chi 2}^{\text{T},ij})$ | $\frac{\sqrt{\rho+\rho_-}}{12\pi s^2\sqrt{\kappa_f}}\{3s[(3-2\kappa_f)\rho_+ + \kappa_f\rho_-] - 2(3-\kappa_f)\rho_+\rho_-\}$, | $\frac{2m_\chi^2}{\pi}(1-\eta_{ij})^2(1+2\eta_{ij})$. |
| Vector DM case A | | |
| $\mathcal{O}_{\ell X}^{\text{S},ij}(\mathcal{O}_{\ell X}^{\text{P},ij})$ | $\frac{\sqrt{\rho+\rho_-}}{1512\pi m_X^4\sqrt{\kappa_f}}(3-2\kappa_f+3\kappa_f^2)\rho_-$, | $\frac{1}{12\pi}(1-\eta_{ij})^2$. |
| $\mathcal{O}_{\ell X 1}^{\text{T},ij}(\mathcal{O}_{\ell X 2}^{\text{T},ij})$ | $\frac{\sqrt{\rho+\rho_-}}{1728\pi m_X^4 s\sqrt{\kappa_f}}\{3s[2(2\kappa_f-\kappa_f^2)\rho_+ + (3-4\kappa_f+\kappa_f^2)\rho_-] - 2(3-\kappa_f^2)\rho_+\rho_-\}$, | $\frac{1}{18\pi}(1-\eta_{ij})^2(1+2\eta_{ij})$. |
| $\mathcal{O}_{\ell X 1}^{\text{V},ij}(\mathcal{O}_{\ell X 1}^{\text{A},ij})$ | $\frac{\sqrt{\rho+\rho_-}}{4320\pi m_X^4 s^2\sqrt{\kappa_f}}\{15s^3[(\kappa_f-\kappa_f^2)\rho_+ + \kappa_f^2\rho_-]$ $- 5s^2[3(\kappa_f-\kappa_f^2)\rho_+^2 + 3\kappa_f^2\rho_-^2 + 4\kappa_f\rho_+\rho_-]$ $+ 10s[(3-2\kappa_f)\rho_+ + (\kappa_f+\kappa_f^2)\rho_-]\rho_+\rho_- - (15-10\kappa_f+3\kappa_f^2)\rho_+\rho_-^2\}$, | $\frac{4m_X^2}{9\pi}(1-\eta_{ij})^4(1+\eta_{ij})$. |
| $\mathcal{O}_{\ell X 2}^{\text{V},ij}(\mathcal{O}_{\ell X 2}^{\text{A},ij})$ | $\frac{\sqrt{\kappa_f\rho+\rho_-}}{864\pi m_X^4}\{3s[(1-\kappa_f)\rho_+ + \kappa_f\rho_-] - (1+2\kappa_f)\rho_+\rho_-\}$, | $\frac{m_X^2}{27\pi}(1-\eta_{ij})^2(2+\eta_{ij})v_{\text{rel}}^2$. |
| $\mathcal{O}_{\ell X 3}^{\text{V},ij}(\mathcal{O}_{\ell X 3}^{\text{A},ij})$ | $\frac{\sqrt{\kappa_f\rho+\rho_-}}{432\pi m_X^2 s}\{3s[2\kappa_f\rho_+ + (1-\kappa_f)\rho_-] - (3-\kappa_f)\rho_+\rho_-\}$, | $\frac{m_X^2}{18\pi}\eta_{ij}(1-\eta_{ij})^2v_{\text{rel}}^2$ $+ \frac{m_X^2}{108\pi}(1-\eta_{ij})(2-\eta_{ij}+2\eta_{ij}^2)v_{\text{rel}}^4$. |
| $\mathcal{O}_{\ell X 4}^{\text{V},ij}(\mathcal{O}_{\ell X 4}^{\text{A},ij})$ | $\frac{\sqrt{\kappa_f\rho+\rho_-}}{3456\pi m_X^4}(3-2\kappa_f+3\kappa_f^2)\rho_+(3s-\rho_-)$, | $\frac{m_X^2}{36\pi}(1-\eta_{ij})^2(2+\eta_{ij})v_{\text{rel}}^2$. |
| $\mathcal{O}_{\ell X 5}^{\text{V},ij}(\mathcal{O}_{\ell X 5}^{\text{A},ij})$ | $\frac{\sqrt{\kappa_f\rho+\rho_-}}{864\pi m_X^4}(2-\kappa_f)\rho_+(3s-\rho_-)$, | $\frac{2m_X^2}{27\pi}(1-\eta_{ij})^2(2+\eta_{ij})v_{\text{rel}}^2$. |
| $\mathcal{O}_{\ell X 6}^{\text{V},ij}(\mathcal{O}_{\ell X 6}^{\text{A},ij})$ | $\frac{\sqrt{\rho+\rho_-}}{432\pi m_X^2 s\sqrt{\kappa_f}}(3-\kappa_f)\rho_+(3s-\rho_-)$, | $\frac{m_X^2}{9\pi}(1-\eta_{ij})^2(2+\eta_{ij})$. |
| Vector DM case B | | |
| $\tilde{\mathcal{O}}_{\ell X 1}^{\text{S},ij}(\tilde{\mathcal{O}}_{\ell X 1}^{\text{P},ij})$ | $\frac{\sqrt{\rho+\rho_-}}{288\pi\sqrt{\kappa_f}}(3+2\kappa_f+3\kappa_f^2)\rho_-$, | $\frac{m_X^4}{3\pi}(1-\eta_{ij})^2$. |
| $\tilde{\mathcal{O}}_{\ell X 2}^{\text{S},ij}(\tilde{\mathcal{O}}_{\ell X 2}^{\text{P},ij})$ | $\frac{\sqrt{\kappa_f\rho+\rho_-}}{36\pi}\rho_-$, | $\frac{2m_X^4}{9\pi}(1-\eta_{ij})^2v_{\text{rel}}^2$. |
| $\tilde{\mathcal{O}}_{\ell X 1}^{\text{T},ij}(\tilde{\mathcal{O}}_{\ell X 2}^{\text{T},ij})$ | $\frac{\sqrt{\rho+\rho_-}}{1728\pi s\sqrt{\kappa_f}}\{3s[2(3\kappa_f-\kappa_f^2)\rho_+ + (3+\kappa_f^2)\rho_-] - 2(3+6\kappa_f-\kappa_f^2)\rho_+\rho_-\}$, | $\frac{m_X^4}{18\pi}(1-\eta_{ij})^2(1+2\eta_{ij})$. |

TABLE II. The annihilation cross section for the process $\text{DM} + \text{DM} \rightarrow \ell_i^- \ell_{j \neq i}^+$ induced by each DSEFT operator with its Wilson coefficient C_i^j , for the case of a complex scalar/vector and Dirac fermion DM field. For the σ in the second column, the expression for the operators in round brackets is obtained by $\rho_- \leftrightarrow \rho_+$. For σv_{rel} , we have neglected the lighter lepton's mass and kept the leading-order results in the expansion of v_{rel}^2 . Note that $\eta_{ij} \equiv \max[m_i^2, m_j^2]/(4m_{\text{DM}}^2)$. In the real scalar/vector and Majorana fermion DM cases, the above results for σ and σv_{rel} from nonvanishing operators need to be multiplied by a factor of 4.

$$t_+ = 2m_{\text{DM}}^2 + m_i^2 + m_j^2 - s. \quad (2b)$$

Here, $\lambda(x, y, z) = x^2 + y^2 + z^2 - 2(xy + yz + zx)$ denotes the triangle function. Defining $\rho_\pm \equiv s - (m_i \mp m_j)^2$, it follows that $\lambda(s, m_i^2, m_j^2) = \rho_+\rho_-$. The total cross section induced by each DSEFT operator can be calculated directly from Eq. (1), and the final results are summarized in the second column of Table II. In the table, $\kappa_f \equiv 1 - 4m_{\text{DM}}^2/s = \lambda(s, m_{\text{DM}}^2, m_{\text{DM}}^2)/s^2$. Since DM particles annihilate non-relativistically, it is a good approximation to expand the velocity-weighted cross-section in terms of the DM relative velocity v_{rel} to simplify subsequent calculations. In the center-of-mass

frame, $s = 4m_{\text{DM}}^2[1 + v_{\text{rel}}^2/(4 - v_{\text{rel}}^2)] = 4m_{\text{DM}}^2[1 + v_{\text{rel}}^2/4 + v_{\text{rel}}^4/16 + \mathcal{O}(v_{\text{rel}}^6)]$ in the nonrelativistic limit. Consequently, σv_{rel} can be Taylor-expanded in powers of v_{rel}^2 as $\sigma v_{\text{rel}} = \hat{a} + \hat{b}v_{\text{rel}}^2 + \hat{d}v_{\text{rel}}^4 + \mathcal{O}(v_{\text{rel}}^6)$, where \hat{a} , \hat{b} , and \hat{d} denote the s-, p-, and d-wave contributions, respectively. The leading-order expansion results of σv_{rel} are tabulated in the third column of Table II.

We make a few comments on the results. First, the calculation of the squared matrix elements for the process $\text{DM} + \text{DM} \rightarrow \ell_i^- \ell_j^+$, induced by the DSEFT operators, is performed using **FeynCalc** package [28], followed by the phase space integration. Second, in the Galactic

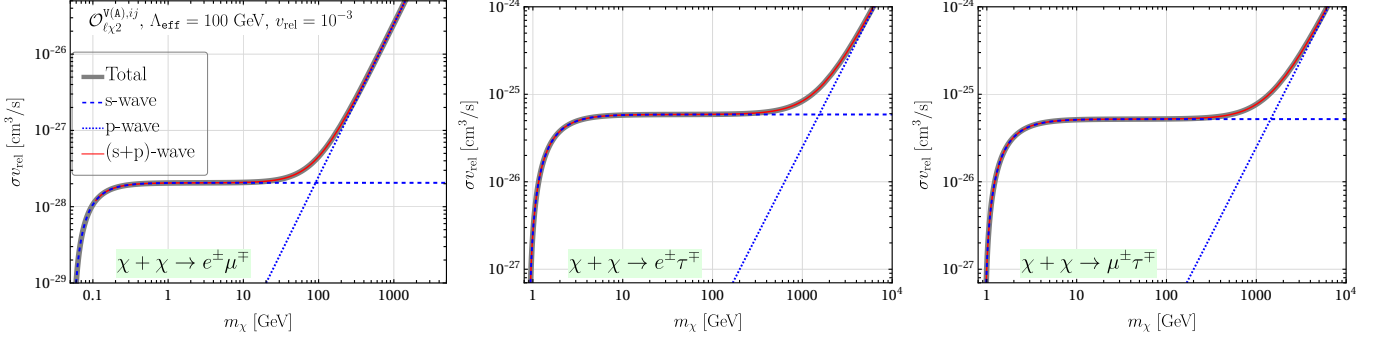


FIG. 1. Comparison of σv_{rel} as a function of m_{DM} between the full calculation (thick gray curve) and the partial-wave components for the operators $\mathcal{O}_{\ell\chi 2}^{\text{V(A)},ij}$. In the plots, we use typical values of $v_{\text{rel}} = 10^{-3}$ and $\Lambda_{\text{eff}} = 100$ GeV. Similar behavior applies to the vector DM operators $\mathcal{O}_{\ell X 3}^{\text{V(A)},ij}$, where the labels ‘s-wave’ and ‘p-wave’ are replaced by ‘p-wave’ and ‘d-wave’, respectively.

DM halo, the typical DM velocity is approximately $10^{-3}c$ where c is the speed of light, implying that DM is highly non-relativistic. It is therefore reasonable to expand σv_{rel} in terms of v_{rel}^2 and keep the leading-order terms. From the last column in the table, one observes that the scalar DM operators $\mathcal{O}_{\ell\phi}^{\text{S(P)}}$ ($\mathcal{O}_{\ell\phi}^{\text{V(A)}}$) lead to annihilation processes that are dominated by s (p)-wave, due to the DM current structure. In the case of fermion DM, every operator contributes primarily through s-wave annihilation except $\mathcal{O}_{\ell\chi 1}^{\text{S(P)}}$, which instead produce a p-wave dominated contribution. For the vector DM case A (B), contributions to σv_{rel} from operators $\mathcal{O}_{\ell X}^{\text{S(P)}}$, $\mathcal{O}_{\ell X 1,2}^{\text{T}}$, and $\mathcal{O}_{\ell X 6}^{\text{V(A)}}$ ($\tilde{\mathcal{O}}_{\ell X 1}^{\text{S(P)}}$ and $\tilde{\mathcal{O}}_{\ell X 1,2}^{\text{T}}$) are s-wave dominated, whereas the remaining operators $\mathcal{O}_{\ell X 1,2,3,4}^{\text{V(A)}}$ ($\tilde{\mathcal{O}}_{\ell X 2}^{\text{S(P)}}$) contribute predominantly through p-wave annihilation. Lastly, for the operators $\mathcal{O}_{\ell\chi 2}^{\text{V(A)}}$ ($\mathcal{O}_{\ell X 3}^{\text{V(A)}}$) in the fermion (vector) case, it is necessary to include both the leading and next-to-leading order expansion to accurately capture the behavior of the full calculation. This is because their leading-order term is proportional to the lepton mass squared via $\eta_{ij} \equiv \max[m_i^2, m_j^2]/(4m_{\text{DM}}^2)$, and the next-to-leading order term becomes dominant when $m_{\text{DM}} \gg \max[m_i, m_j]/v_{\text{rel}}$. For illustration, Fig. 1 compares the contributions to σv_{rel} from different partial waves with the full calculation for the fermion DM operators $\mathcal{O}_{\ell\chi 2}^{\text{V(A)}}$ at a fixed velocity $v_{\text{rel}} = 10^{-3}$. The left, middle, and right panels display the results for the three annihilation modes corresponding to $e\mu$, $e\tau$, and $\mu\tau$ flavor combinations, respectively. As shown in the left (middle or right) panel, the s-wave contribution is valid only when the DM mass is below $m_{\mu(\tau)}/v_{\text{rel}}$, whereas the p-wave contribution becomes significant when $m_{\text{DM}} \gtrsim m_{\mu(\tau)}/v_{\text{rel}}$.

C. Thermally averaged cross sections $\langle \sigma v_{\text{rel}} \rangle$

Since the DM phase space distribution in the galaxy is a function of both position and velocity, and the ob-

served cosmic-ray signal represents a statistical average over all velocity states, it is therefore convenient to define a position-dependent thermally averaged annihilation cross section $\langle \sigma v_{\text{rel}} \rangle(\mathbf{r})$ as follows:

$$\langle \sigma v_{\text{rel}} \rangle(\mathbf{r}) \equiv \int d^3\mathbf{v}_1 f(\mathbf{r}, \mathbf{v}_1) \int d^3\mathbf{v}_2 f(\mathbf{r}, \mathbf{v}_2) \sigma v_{\text{rel}}, \quad (3)$$

where \mathbf{r} denotes the DM annihilation position in the galactic frame. The DM velocity distribution $f(\mathbf{r}, \mathbf{v})$ at position \mathbf{r} is approximated by a normalized, isotropic Maxwell–Boltzmann distribution with a velocity dispersion $v_0(r)$ [29–31], which is r -dependent and can be obtained by solving the Jeans equation [32, 33]. According to the nonrelativistic expansion, $\sigma v_{\text{rel}} = \hat{a} + \hat{b} v_{\text{rel}}^2 + \hat{d} v_{\text{rel}}^4 + \dots$, the thermal average becomes

$$\langle \sigma v_{\text{rel}} \rangle(r) = \hat{a} + 6\hat{b} v_0^2(r) + 60\hat{d} v_0^4(r) + \dots, \quad (4)$$

which is also isotropic and $v_0(r)$ -dependent for p- and d-wave contributions. More details for the derivation are given in Section A.

III. CALCULATION OF THE PHOTON AND POSITRON SPECTRA

In our analysis, the relevant observational signals include diffuse photons and positrons. Below, we detail their primary production mechanisms from DM origins and the calculation of the spectra at Earth after accounting for the astrophysical propagation effects.

A. Photon flux

We begin with the calculation of the photon flux. The diffuse X/gamma-ray background from DM annihilation in the Universe has two main contributions: the localized galactic component and the extra-galactic component due to the smooth DM distribution throughout

the Universe. For telescopes relevant to our discussion, the Milky Way's DM halo provides the dominant contribution; therefore, we neglect the subdominant extragalactic contribution. For LFV DM-lepton operators in Table I, the induced photon flux is mainly generated through three mechanisms: final state radiation (FSR) via the three-body annihilation $\text{DM} + \text{DM} \rightarrow \ell_i^\pm \ell_j^\mp \gamma$, radiative decay (Rad) of final state leptons in the two-body annihilation $\text{DM} + \text{DM} \rightarrow \ell_i^\pm \ell_j^\mp$, and inverse Compton scattering (ICS) of background soft photons up-scattered by energetic e^\pm generated in the two-body annihilation and subsequent decays of μ and/or τ leptons. The first two correspond to the so-called prompt photons, while the ICS photons are nonprompt. The total differential photon flux is a sum of them

$$\frac{d^2\Phi_\gamma}{d\Omega dE_\gamma} = \frac{d^2\Phi_\gamma^{\text{FSR}}}{d\Omega dE_\gamma} + \frac{d^2\Phi_\gamma^{\text{Rad}}}{d\Omega dE_\gamma} + \frac{d^2\Phi_\gamma^{\text{ICS}}}{d\Omega dE_\gamma}. \quad (5)$$

For the prompt photons from FSR and Rad, the flux is related to the thermally averaged cross section in Eq. (3) via the following form,

$$\frac{d^2\Phi_\gamma^I}{d\Omega dE_\gamma} = \frac{1}{4\pi} \frac{dN_\gamma^I}{dE_\gamma} \int_{\text{l.o.s.}} \frac{\rho^2(\mathbf{r})}{\mathbf{S}} \frac{\langle \sigma v_{\text{rel}} \rangle_{ij+ji}(\mathbf{r})}{(1 + \delta_{ij})m_{\text{DM}}^2} ds', \quad (6)$$

Here, $\mathbf{S} = 4(2)$ for complex (real) scalar, vector, or Dirac (Majorana) DM particles, reflecting the number of independent combinations of DM annihilation. dN_γ^I/dE_γ denotes the normalized photon spectrum in each annihilation process relative to the corresponding two-to-two annihilation, with I representing either FSR or Rad. The calculation will be detailed below. The integration of s' is along the line of sight (l.o.s) that accounts for all contributions along a specific direction. For the DM distribution $\rho(\mathbf{r})$, we adopt the standard Navarro-Frenk-White (NFW) profile, $\rho_{\text{NFW}}(r) \equiv \rho_s(r/r_s)^{-1}(1 + r/r_s)^{-2}$ [34, 35], where r denotes the distance from the galactic center, and r_s is the scale radius defined by $(d \ln \rho / d \ln r)_{r=r_s} = -2$. Numerically, $r_s = 24.42$ kpc and $\rho_s = 0.184$ GeV/cm³ [36], leading to a local DM density $\rho \approx 0.3$ GeV/cm³. In the galactic coordinate, r is related to the l.o.s distance s' via, $r(s') = \sqrt{r_\odot^2 + s'^2 - 2r_\odot s' \cos \psi}$. Here ψ is the angle between the l.o.s and the direction to the galactic center, $r_\odot = 8.3$ kpc is the distance of Earth to the galactic center, and $\cos \psi \equiv \cos b \cos l$, where b and l are the galactic latitude and longitude, respectively. The integration range for s' is from 0 to a maximal value determined by the virial radius $r_{\text{vir}} = 300$ kpc of the DM halo [37],

$$s'_{\text{max}} = r_\odot \cos \psi + \sqrt{r_{\text{vir}}^2 - r_\odot^2 \sin^2 \psi}. \quad (7)$$

1. Final state radiation

We now proceed to the determination of the FSR photon spectra from operators that yield an s-wave annihilation, which can be readily identified from Table II

as those whose leading-order expansion for σv_{rel} exhibits no velocity suppression. In our calculation, the normalized FSR spectra are obtained from a direct numerical approach. For each s-wave operator, we input the corresponding matrix element for the radiative process $\text{DM} + \text{DM} \rightarrow \ell_i^- \ell_j^+ \gamma$ into the *FeynCalc* package [28] and compute the squared amplitude. This is followed by numerical integration over the final-state lepton phase space for a given DM mass, and division by the flux factor to obtain the differential cross section as a function of the photon's energy in the center-of-mass frame. Finally, the normalized photon spectrum is obtained by dividing the differential cross section $d\sigma(\text{DM} + \text{DM} \rightarrow \ell_i^- \ell_j^+ \gamma)/dE_\gamma$ by the total cross section of the corresponding two-to-two annihilation process $\text{DM} + \text{DM} \rightarrow \ell_i^- \ell_j^+$ mediated by the same operator. The *Mathematica* notebook used to generate the spectra in our analysis is available as auxiliary files from the arXiv source file.

Our numerical results indicate that when the DM mass is significantly greater than the mass of the heavier lepton, all s-wave EFT operators produce nearly identical normalized FSR spectra for a given lepton flavor combination. The differences in their spectra mainly occur as the photon energy approaches its maximum, where the leptonic-current structures of the operators and the masses of the final-state leptons play a significant role. For illustration, Fig. 2 presents a comparison across different operators for three benchmark DM masses in each channel. As observed in the plots, for the typical photon energy below half of its maximum value $E_\gamma^{\text{max}} \equiv m_{\text{DM}} - (m_i + m_j)^2/(4m_{\text{DM}})$, the spectra from different operators become degenerate.

This degenerate behavior for the spectra can be understood analytically as follows. Based on the lepton structure function method [38], the normalized spectra can be approximated by the following analytic expression (see Eq. (14) in that reference)

$$\frac{dN_{ij}^\gamma(x_\gamma, s)}{dx_\gamma} = H_{i,j}(x_\gamma, \hat{s}), \quad \hat{s} \equiv (1 - x_\gamma)s, \quad (8)$$

where s (\hat{s}) denotes the invariant mass squared of the DM pair (lepton pair), and $x_\gamma = E_\gamma/m_{\text{DM}}$. $H_{i,j}(x_\gamma, \hat{s})$ is a final state radiator, which accounts for the radiative corrections to the two-to-two scattering cross section caused by FSR. By extending the LFC result in [38] to our LFV cases, we have

$$H_{i,j}(x_\gamma, \hat{s}) = \int_{1-x_\gamma}^1 \frac{dz}{z} D_i(z, \hat{s}) D_j\left(\frac{1-x_\gamma}{z}, \hat{s}\right). \quad (9)$$

Here, $D_i(x, \hat{s})$ denotes the structure function of the lepton i at the scale \hat{s} with a longitudinal momentum fraction of x . Its exact expression up to $\mathcal{O}(\alpha^2)$ is given in Eq. (3) of Ref. [38]. Expanding the $D_{i,j}$ -function to the linear order in the fine structure constant α , we obtain

$$H_{i,j}(x_\gamma, \hat{s}) = d(x_\gamma, \hat{s}, m_i) + d(x_\gamma, \hat{s}, m_j), \quad (10)$$

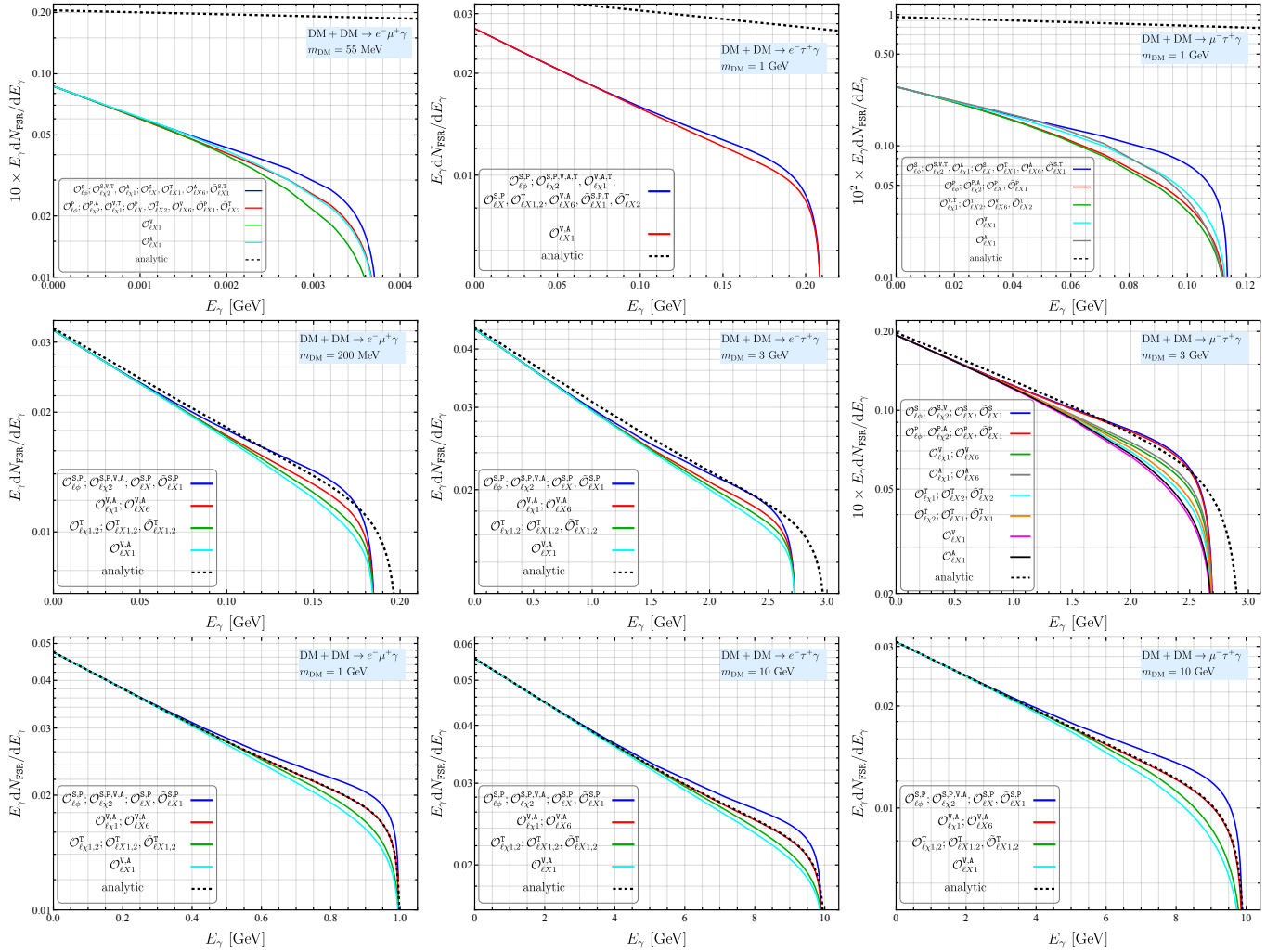


FIG. 2. Comparison of normalized FSR spectra across various s-wave operators and different benchmark DM masses for the three LFV annihilation channels. The dashed curves represent the analytical calculation based on Eq. (10).

where

$$d(x_\gamma, \hat{s}, m_\ell) = \frac{\alpha}{2\pi} (\log[\hat{s}/m_\ell^2] - 1) \frac{1 + (1 - x_\gamma)^2}{x_\gamma}. \quad (11)$$

As shown by the black dashed curves in Fig. 2, the spectra obtained from Eq. (10), which is essentially operator-independent, agree very well with our direct numerical calculation when $m_{\text{DM}} \gg (m_i + m_j)/2$ and $E_\gamma \lesssim E_{\text{DM}}/2$. Even in the high energy tail where $E_\gamma \gtrsim E_{\text{DM}}/2$, the differences remain below 20 %.

Before closing this subsection, we make two additional remarks. First, for operators that share the same Lorentz structure but involve different flavor combinations, the normalized FSR spectrum for each LFV annihilation mode with $\ell_i^- \ell_j^+ \gamma$ final states always lies between those of the two LFC modes involving $\ell_i^- \ell_i^+ \gamma$ and $\ell_j^- \ell_j^+ \gamma$ ($j \neq i$), where the mode containing the lighter lepton pair dominates. The solid curves in Fig. 3 show the FSR spectra for the six channels of lepton flavor, which are calculated based on the operator $\ell_i \gamma_\mu \gamma_5 \ell_j \bar{\chi} \gamma^\mu \gamma_5 \chi$ with

three benchmark DM masses: 3 GeV (left panel), 30 GeV (middle panel), and 300 GeV (right panel). As clearly illustrated by the plots, both LFV and LFC annihilation modes produce FSR spectra with similar shapes. Second, we do not include FSR contributions from operators associated with p- and d-waves, as their calculation depends nontrivially on the DM velocity distribution. A detailed treatment of these contributions is beyond the scope of this work, and is reserved for our future work. Fortunately, in most cases these contributions are subdominant. The only exception occurs in the $e\mu$ channel for a DM mass less than about 4 GeV in which case our constraints derived from photon data for p- and d-wave cases should be regarded conservative, as shown in Fig. 6 below.

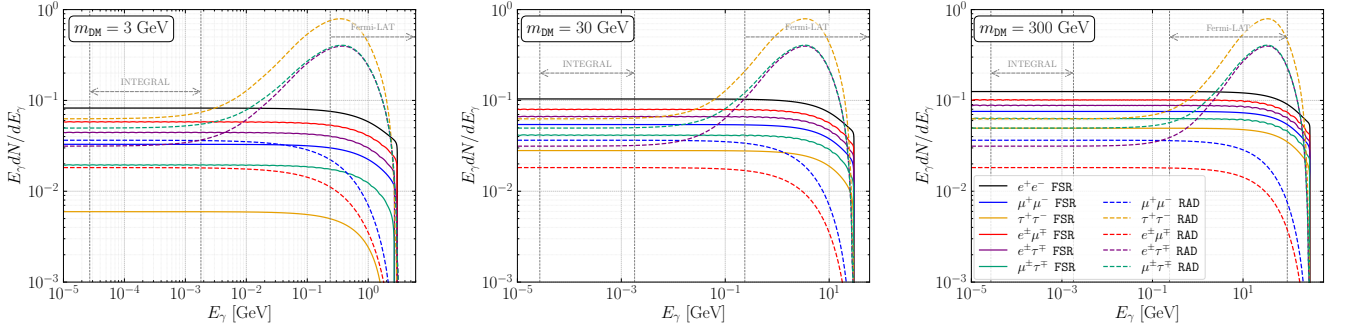


FIG. 3. Comparison of photon spectra for different annihilation channels, including both LFV and LFC cases. The FSR spectra are shown as solid curves, while the Rad spectra are represented by dashed curves. The left, middle, and right panels correspond to DM masses of 3 GeV, 30 GeV, and 300 GeV, respectively.

2. Radiative decays

The Rad photons arise from the radiative decays of the primary charged leptons, μ^\pm and τ^\pm , produced in DM annihilation, and are independent of EFT operators. For the muon, the dominant radiative decay process is $\mu^- \rightarrow e^- \bar{\nu}_e \nu_\mu \gamma$, whereas for the τ lepton, both the leptonic decay modes $\tau^- \rightarrow e^- (\mu^-) \bar{\nu}_{e(\mu)} \nu_\tau \gamma$ and hadronic decay channels contribute significantly. For the four-body leptonic decay process $\ell^- \rightarrow \ell'^- \bar{\nu}_{\ell'} \nu_\ell \gamma$ (and its charge-conjugation counterpart), the Rad photon spectrum can be calculated analytically and is given by [39],

$$\frac{dN_\gamma^{\text{Rad},\ell}}{dE_\gamma^*} = \frac{\alpha(1-x_\ell)}{36\pi E_\gamma^*} \left\{ x_\ell(1-x_\ell)(46-55x_\ell) - 102 + 12[3-2x_\ell(1-x_\ell)^2] \ln \frac{1-x_\ell}{r_{\ell\ell'}} \right\}, \quad (12)$$

where E_γ^* is the photon energy in the lepton rest frame, $x_\ell = 2E_\gamma^*/m_\ell$, and $r_{\ell\ell'} = (m_{\ell'}/m_\ell)^2$ with $\ell\ell' = (\mu e, \tau e, \tau \mu)$ for the three LFV annihilation modes.

For the hadronic radiative decays of the τ lepton, no analytical formulas exist for the resulting photon spectrum. Instead, we obtain it through a detailed PYTHIA simulation [40]. We generate 10^5 τ^- leptons at rest using PYTHIA, collect the final-state photons from their decay products, and bin them according to the photon energy to obtain the normalized spectrum. We find that the leptonic radiative decay modes $\tau^- \rightarrow e^- (\mu^-) \bar{\nu}_{e(\mu)} \nu_\tau \gamma$ are not included in the PYTHIA simulation. Therefore, we combine the simulated photon spectrum with the analytic expressions in Eq. (12) for these leptonic modes to derive the total radiative decay spectrum for τ decay at rest, $dN_\gamma^{\text{Rad},\tau}/dE_\gamma^*$.

For the produced charged lepton ℓ moving in motion, the photon spectrum discussed above in its rest frame need to be boosted to the DM rest frame, which is given by

$$\frac{dN_\gamma^{\text{Rad},\ell}}{dy} = \int_y^1 \frac{d\omega}{\omega} \frac{dN_\gamma^{\text{Rad},\ell}}{d\omega}, \quad (13)$$

where $y \equiv E_\gamma/\sqrt{E_\ell^2 - m_\ell^2}$ and $\omega \equiv E_\gamma^*/(2m_\ell)$. In the DM annihilation channel $\text{DM} + \text{DM} \rightarrow \ell_i^- \ell_j^+$, $\ell = \ell_i^-, \ell_j^+$, and the energies of the charged leptons are

$$E_{i,j} = m_{\text{DM}} \pm \frac{m_i^2 - m_j^2}{4m_{\text{DM}}}. \quad (14)$$

The dashed lines in Fig. 3 show the Rad spectra for the three benchmark DM masses used for the FSR calculation. For a given LFV channel $\ell_i^- \ell_j^+$, the normalized spectrum from Rad also falls between those of the corresponding LFC channels $\ell_i^- \ell_i^+$ and $\ell_j^- \ell_j^+$, with the Rad contribution vanishing for the e^+e^- pair. Unlike in the case of FSR, the dominant contribution now comes from the heavier lepton pair. Since the FSR mainly originates from the collinear and soft photon emission of energetic final-state lighter leptons, its contribution is enhanced in the lower photon energy tail. Consequently, increasing the DM mass, which makes the final-state leptons more energetic, enhances collinear and soft radiation, resulting in a more significant FSR contribution. In contrast, photons from τ leptons are predominantly produced through hadronic τ decays and carry substantial energies. As a result, for LFV channels involving τ leptons ($e\tau$ and $\mu\tau$), the Rad contribution dominates in the high-energy region. In the low-energy region, the FSR contribution dominates for all three benchmark DM masses in the $e\tau$ channel, while for the $\mu\tau$ channel it dominates only when $m_{\text{DM}} \gtrsim 300$ GeV. Finally, it should be noted that the FSR always dominates over the Rad in the photon spectrum for the $e\mu$ case.

3. The inverse Compton scattering

In addition to the FSR and Rad photons, the ICS photons—produced primarily by the scattering of high-energy e^\pm s from DM annihilation off the galactic background low energy photons—dominate the photon flux at lower photon energies, as will be shown below. The background photons mainly consist of the cosmic microwave background (CMB), optical starlight emitted by stars in

the galactic disk, and infrared light resulting from the absorption and re-emission of starlight by galactic dust. The ICS flux can be written as an integral of the photon emissivity $j(E_\gamma, \mathbf{r})$ at position \mathbf{r} in the galactic coordinate, along the l.o.s direction,

$$\frac{d^2\Phi_\gamma^{\text{ICS}}}{d\Omega dE_\gamma} = \frac{1}{4\pi} \int_{\text{l.o.s.}} ds' \frac{j(E_\gamma, \mathbf{r})}{E_\gamma}. \quad (15)$$

The emissivity characterizes the photon emission capability of a cell at \mathbf{r} and is obtained by convolving the e^\pm spectral number density (dn_{e^\pm}/dE_e) with the corresponding differential radiation power into photons ($\mathcal{P}_{\text{ICS}}(E_\gamma, E_e, \mathbf{r})$),

$$j(E_\gamma, \mathbf{r}) = \int_{m_e}^{E_e^{\text{max}}} dE_e \mathcal{P}_{\text{ICS}}(E_\gamma, E_e, \mathbf{r}) \frac{dn_{e^\pm}}{dE_e}(E_e, \mathbf{r}), \quad (16)$$

where the maximum energy of the electron or positron is determined by the kinematics of DM annihilation, with $E_e^{\text{max}} = \max[E_i, E_j]$, where $E_{i,j}$ are given in Eq. (14).

The e^\pm spectral distribution dn_{e^\pm}/dE_e includes contributions from both electrons and positrons produced through the annihilation channel $\text{DM} + \text{DM} \rightarrow \ell_i^- \ell_j^+$ and the subsequent decays of charged muons and taus. It relates to the e^\pm phase-space distribution function $f_e(p, \mathbf{r})$ via the relation $dn_{e^\pm}/dE_e = 4\pi E_e p f_e(p, \mathbf{r})$, where p and E_e denote the magnitude of the momentum and the energy of e^\pm , respectively. The function $f_e(p, \mathbf{r})$ is governed by a transport equation, whose main components include a diffusion term, an energy loss term, and an e^\pm -source term [41]. In addition, two other terms — advection and convection — describe the flow of e^\pm s near the Galactic center; however, their effect can be safely neglected in the region of interest for DM annihilation and observation [42].

Furthermore, following Ref. [43], we adopt the “on the spot” approximation in our analysis. This implies neglecting the diffusion term and assuming that the scattering occurs exactly at the location where these e^\pm s are produced from DM annihilation. It is anticipated that diffusion would partially redistribute the e^\pm population from regions of high DM density to areas of lower density, effectively shifting the photon flux generated by ICS from the galactic center region toward larger radii. Refs. [42, 44] demonstrate that the flux predicted by fully numerical GALPROP calculations [45, 46] agrees with the “on the spot” approximation within a factor of two, making this approximation reasonably accurate. By neglecting the diffusion term, the e^\pm spectral distribution can then be solved semi-analytically,

$$\frac{dn_{e^\pm}}{dE_e}(E_e, \mathbf{r}) = \frac{Y_{e^\pm}(E_e)}{b_{\text{tot}}(E_e, \mathbf{r})} \frac{\langle \sigma v_{\text{rel}} \rangle_{ij+ji}(\mathbf{r})}{S(1 + \delta_{ij})m_{\text{DM}}^2} \rho^2(\mathbf{r}), \quad (17)$$

where $b_{\text{tot}}(E_e, \mathbf{r})$ represents the total energy loss function of the e^\pm s [47], including contributions from synchrotron radiation, bremsstrahlung, ionization, and ICS. We adopt

the numerical interpolation function provided by PPPC4 [36] in our calculation. $Y_{e^\pm}(E_e)$ is defined by

$$Y_{e^\pm}(E_e) \equiv \int_{E_e}^{E_e^{\text{max}}} d\tilde{E}_e \frac{dN_{e^\pm}}{d\tilde{E}_e}(\tilde{E}_e). \quad (18)$$

Here, $dN_{e^\pm}/d\tilde{E}_e$ is the energy spectrum of e^\pm s produced per DM annihilation event in the DM rest frame, including contributions from the primary e^\pm (when $\ell_i^- = e^-$ or $\ell_j^+ = e^+$) and the secondary ones due to decays of μ and τ . The spectrum of primary e^\pm is simply represented by a Dirac delta function. For muon decay at rest, the e^\pm spectrum is determined by the process $\mu^- \rightarrow e^- \nu_\mu \bar{\nu}_e$ and its conjugate. For τ decay at rest, we obtain the e^\pm spectra using PYTHIA8 simulations. Similarly to the Rad component of the photon flux, we need to boost the e^\pm spectrum in the lepton rest frame to the DM rest frame via

$$\frac{dN_{e^\pm}}{d\tilde{E}_e} = \frac{1}{2\beta_\ell \gamma_\ell} \int_{E_{\min}^*}^{E_{\max}^*} \frac{dN_{e^\pm}}{dE_e^*} \frac{dE_e^*}{p_e^*}, \quad (19)$$

where $\gamma_\ell = E_\ell/m_\ell$ is the Lorentz boost factor of the parent lepton ℓ , $\beta_\ell = (1 - 1/\gamma_\ell^2)^{1/2}$, and $p_e^* = \sqrt{(E_e^*)^2 - m_e^2}$. The integration limits are given by $E_{\max(\min)}^* = \gamma_\ell(\tilde{E}_e \pm \beta_\ell \tilde{p}_e)$ with $\tilde{p}_e = \sqrt{\tilde{E}_e^2 - m_e^2}$.

Next, we turn to the function \mathcal{P}_{ICS} , which physically represents the scattering rate of high energy e^\pm interacting with background photons. It can be expressed as

$$\mathcal{P}_{\text{ICS}} = \int d\epsilon_\gamma (E_\gamma - \epsilon_\gamma) \frac{dn_\gamma}{d\epsilon_\gamma}(\epsilon_\gamma, \mathbf{r}) \frac{d\sigma_{\text{eff}}}{dE_\gamma}(\epsilon_\gamma, E_\gamma, E_e). \quad (20)$$

Here, ϵ_γ denotes the energy of background photons with the number density spectrum $dn_\gamma/d\epsilon_\gamma$ which comprises the three components described above. The isotropic CMB component follows a thermal Bose-Einstein distribution at a temperature $T = 2.73$ K. For the infrared and starlight components, we employ the data provided in GALPROP [48]. $d\sigma_{\text{eff}}/dE_\gamma$ denotes an effective ICS cross section that incorporates the effects of Lorentz boosts and frame transformations. Its expression can be derived from Eq. (2.48) of Ref. [47], with appropriate adjustments to account for differences in notation,

$$\frac{d\sigma_{\text{eff}}}{dE_\gamma} = \frac{3\sigma_T}{4\gamma^2 \epsilon_\gamma} \left[2q \ln q + q + 1 - 2q^2 + \frac{1}{2} \frac{\kappa_\gamma^2}{1 - \kappa_\gamma} (1 - q) \right], \quad (21)$$

where $\kappa_\gamma \equiv E_\gamma/(\gamma m_e)$, and $q \equiv \kappa_\gamma/[\Gamma_\epsilon(1 - \kappa_\gamma)]$ with $\Gamma_\epsilon \equiv 4\epsilon_\gamma \gamma/m_e$. $\gamma = E_e/m_e$ is the Lorentz boost factor of the electron or positron in the reference frame of the photon gas. $\sigma_T = 0.6652$ barn is the total Thomson cross section. Trading the integral variable ϵ_γ by the dimensionless q -variable, the final differential power \mathcal{P}_{ICS} takes the following form,

$$\mathcal{P}_{\text{ICS}} = \sigma_T E_\gamma \int_{\frac{1}{4\gamma^2}}^1 dq \frac{dn_\gamma}{d\epsilon_\gamma}(\epsilon_\gamma(q), \mathbf{r}) f_{\text{ICS}}(q), \quad (22)$$

where

$$f_{\text{ICS}} \equiv \frac{3}{4\gamma^2} \left[1 - \frac{1}{4q\gamma^2(1-\kappa_\gamma)} \right] \times \frac{1}{q} \times \left[2q \ln q + q + 1 - 2q^2 + \frac{1}{2} \frac{\kappa_\gamma^2}{1-\kappa_\gamma} (1-q) \right]. \quad (23)$$

4. Comparison of photon flux

Having detailed the three main photon sources, it is enlightening to compare their relative contributions to the produced photon flux in various scenarios. In Fig. 4, we show the predicted photon fluxes for the three LFV channels from the three photon components: FSR (red curves), Rad (blue curves), and ICS (green curves). The fluxes are calculated based on a Dirac DM scenario for two benchmark DM masses: $m_{\text{DM}} = 3 \text{ GeV}$ (solid curves) and 300 GeV (dashed curves). The values of $\langle \sigma v_{\text{rel}} \rangle = \langle \sigma v_{\text{rel}} \rangle_{ij+ji}$ are fixed at $3 \times 10^{-26} \text{ cm}^3/\text{s}$ and $3 \times 10^{-24} \text{ cm}^3/\text{s}$ for the two mass points, respectively. In the calculation, we choose a sky region with $8^\circ < |b| < 90^\circ$ and $0 < l < 360^\circ$, which corresponds to the observation window of Fermi-LAT.

As shown in the plots, the photon spectra exhibit distinct behavior for the different radiation components, reflecting their underlying production mechanisms. In the low-energy range (keV–100 MeV), ICS dominates for all three LFV channels. This is because electrons and positrons produced in GeV-scale DM annihilation already carry sufficient energy to upscatter low-energy background photons into the X-ray range, resulting in the ICS flux that greatly exceeds those from Rad and FSR. In the high energy range (100 MeV–10 GeV), the dominant contribution depends on both annihilation channel and DM mass. For τ -related channels ($e\tau$ and $\mu\tau$), Rad dominates in both the light and heavy DM scenarios, as hadronic τ decays produce energetic photons. In the $e\mu$ channel, the dominant component varies with DM mass: FSR prevails in the light DM region, while ICS becomes dominant in the heavy DM region. These features highlight the complementary roles played by the three photon components across different energy ranges. More importantly, they will help us to understand the final constraints presented in the next section.

B. Positron flux

Taking into account both energy losses and spatial diffusion, the solution of the transport equation leads to the positron flux from DM annihilation given by [36]:

$$\frac{d\Phi_{e+}}{dE_e}(E_e, \mathbf{r}) = \int_{E_e}^{E_e^{\text{max}}} d\tilde{E}_e \frac{Q_e(\tilde{E}_e, \mathbf{r}) I(E_e, \tilde{E}_e, \mathbf{r})}{4\pi b_{\text{tot}}(E_e, \mathbf{r})}, \quad (24)$$

where the positron source term Q_e is related to the DM annihilation cross section through the relation

$$Q_e(\tilde{E}_e, \mathbf{r}) = \frac{dN_{e+}}{d\tilde{E}_e} \frac{\langle \sigma v_{\text{rel}} \rangle_{ij+ji}(\mathbf{r})}{\mathbf{S}(1 + \delta_{ij})m_{\text{DM}}^2} \rho^2(\mathbf{r}). \quad (25)$$

Here, $dN_{e+}/d\tilde{E}_e$ is half of the spectrum in Eq. (19), since only positrons contribute to the signal from the ij and ji modes with the assumption $\langle \sigma v_{\text{rel}} \rangle_{ij} = \langle \sigma v_{\text{rel}} \rangle_{ji}$. $I(E_e, \tilde{E}_e, \mathbf{r})$ in Eq. (24) is a generalized dimensionless halo function that describes the probability of observing a positron with energy E_e at position \mathbf{r} , after it has been injected with energy \tilde{E}_e . We evaluate the expression at $\mathbf{r} = \mathbf{r}_\odot$ with \mathbf{r}_\odot being the location of the Sun and use the corresponding interpolation halo function $I(E_e, \tilde{E}_e, \mathbf{r}_\odot)$ offered in [36].

IV. CONSTRAINTS

We employ four complementary datasets to derive our constraints, including three X-/gamma-ray telescopes—INTEGRAL, XMM-Newton, and Fermi-LAT, together with a cosmic-ray positron dataset measured by AMS-02. Their sensitive energy ranges and sky coverages are summarized in Table III. INTEGRAL data are taken from Ref. [25], covering photon energies from 27 to 1800 keV. The fluxes are provided in latitude bins and integrated over $|l| < 23.1^\circ$ for energies below 600 keV, and over $|l| < 60^\circ$ for energies between 600 and 1800 keV. For XMM-Newton, we use the publicly available all-sky dataset from the MOS and PN cameras [26, 49], excluding the latitude region $|b| \leq 2^\circ$. To suppress dominant instrumental backgrounds, the energy range used in the analysis is restricted to 2.5–8 keV for the MOS camera and 2.5–7 keV for the PN camera [26]. We adopt the Fermi-LAT 2012 dataset [24] in the energy range 200 MeV–10 GeV, covering the sky region $0 < l < 360^\circ$ and $8^\circ < |b| < 90^\circ$. Finally, we use the AMS-02 positron spectrum measured up to 1 TeV from [27], restricting the analysis to energies above 20 GeV to suppress solar modulation effects. Further details for these datasets can be found in [23]. Please note that the XMM-Newton dataset is publicly accessible online at [49], while the datasets we extracted from INTEGRAL, Fermi-LAT, and AMS-02 are available in the ancillary files of the arXiv version of our previous work [23].

In our analysis, we neglect astrophysical background components due to their large uncertainties and assume that all observed fluxes originate from DM annihilation in order to derive a conservative limit. It is expected that a dedicated analysis including background contributions will lead to more stringent bounds. Following Refs. [43, 50], we use a conservative chi-square test to derive our constraints:

$$\chi^2 \equiv \sum_i \left(\frac{\max[S_i(w, m_{\text{DM}}) - O_i, 0]}{\sigma_i} \right)^2, \quad (26)$$

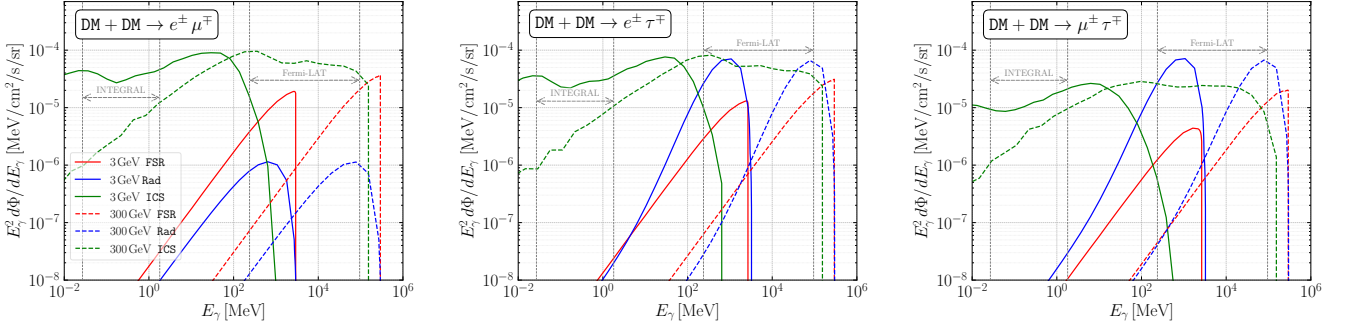


FIG. 4. Photon fluxes from FSR (red), Rad (blue), and ICS (green) are shown for the three LFV DM annihilation channels. The solid and dashed curves correspond to $m_{\text{DM}} = 3$ GeV and 300 GeV, respectively. The gray vertical dashed lines denote the energy ranges covered by INTEGRAL and Fermi-LAT. We fix $\langle \sigma v_{\text{rel}} \rangle_{ij+ji}$ to 3×10^{-26} and $3 \times 10^{-24} \text{ cm}^3/\text{s}$ for $m_{\text{DM}} = 3$ and 300 GeV cases, respectively, and adopt the sky region for the Fermi-LAT dataset ($8^\circ < |b| < 90^\circ$, $0 < l < 360^\circ$).

| Experiment | Data energy range | Sky coverage | Data source |
|------------|-------------------|---|----------------|
| INTEGRAL | 27–1800 keV | $ l < 23.1^\circ$ ($E_\gamma < 600$ keV); $ l < 60^\circ$ (600 keV $< E_\gamma < 1800$ keV) | Ref. [25] |
| XMM-Newton | 2.5–8 keV | All sky excluding $ b \leq 2^\circ$ | Refs. [26, 49] |
| Fermi-LAT | 200 MeV–10 GeV | $0 < l < 360^\circ$, $8^\circ < b < 90^\circ$ | Ref. [24] |
| AMS-02 | 20 GeV–1 TeV | — | Ref. [27] |

TABLE III. Summary of the datasets used in this work, including the energy range, sky coverage, and data sources for each experiment.

where S_i and O_i are the DM-induced and observed photon fluxes or event counts in the i -th bin with uncertainty σ_i . Here, $w = \hat{a}$, \hat{b} , and \hat{d} for deriving constraints on the general thermally averaged cross section for s-, p-, and d-wave cases, respectively, while $w = \Lambda_{\text{eff}}$ applies in the case of EFT operators. For each DM mass point, we derive the 2σ bound on the parameter w by requiring $\chi^2 = 4$.

A. General constraints on $\langle \sigma v_{\text{rel}} \rangle$

As discussed in the previous section and illustrated in Fig. 4, the three components of the photon signal exhibit varying relative magnitudes depending on the DM mass, the annihilation channel, and the photon energy range. The telescopes INTEGRAL and Fermi-LAT are sensitive to low-energy and high-energy photons, respectively; making them complementary to each other. Motivated by this complementarity, in Fig. 5, we present a comparison of the constraints on the s-wave $\langle \sigma v_{\text{rel}} \rangle$ from the three photon components—FSR (red curves), Rad (blue curves), and ICS (green curves)—through the INTEGRAL (solid curves) and Fermi-LAT (dashed curves) datasets. The behavior of the constraints in Fig. 5 can be directly understood in relation to the photon flux comparison presented in Fig. 4. In particular, owing to the significant X-ray flux induced by ICS, the INTEGRAL constraints derived from the ICS component provide the strongest limits for all three LFV channels in the mass range

$m_{\text{DM}} \lesssim 50$ GeV. In the higher mass region, $m_{\text{DM}} \gtrsim 50$ GeV, the constraints are instead dominated by Fermi-LAT. In this regime, ICS remains the most important component for the photon flux in the $e\mu$ channel, while the dominant contribution shifts to the Rad component for the τ -related channels ($e\tau$ and $\mu\tau$).

In Fig. 6, we present the final constraints on $\langle \sigma v_{\text{rel}} \rangle$ related to the s-, p-, and d-wave contributions, indicated by the solid, dashed, and dotted curves, respectively. The constraints derived from INTEGRAL, XMM-Newton, Fermi-LAT, and AMS-02 are represented by red, green, blue, and magenta curves, respectively. For the photon telescope experiments (INTEGRAL, XMM-Newton, and Fermi-LAT), the constraints in the s-wave case are derived by combining all three photon components, while in the p- and d-wave cases conservative constraints are obtained by disregarding the FSR component for the reason that we mentioned in Section III A 1. The results for the three partial wave components are evaluated according to the nonrelativistic expansion $\sigma v_{\text{rel}} = \hat{a} + \hat{b} v_{\text{rel}}^2 + \hat{d} v_{\text{rel}}^4 + \dots$. We derive the 2σ constraints on \hat{a} , \hat{b} , and \hat{d} , which are denoted as $\hat{a}_{2\sigma}$, $\hat{b}_{2\sigma}$, and $\hat{d}_{2\sigma}$ for the s-, p-, and d-wave contributions, respectively. We find that the ratios $\hat{a}_{2\sigma}/\hat{b}_{2\sigma}$ and $\hat{a}_{2\sigma}/\hat{d}_{2\sigma}$ across the entire mass range can be largely accounted for by two constant velocity-suppression factors: $(v_{\text{ref}}^{\text{p}})^2$ and $(v_{\text{ref}}^{\text{d}})^4$. This suggests, with good approximation, that

$$\hat{a}_{2\sigma} \simeq \hat{b}_{2\sigma} (v_{\text{ref}}^{\text{p}})^2 \simeq \hat{d}_{2\sigma} (v_{\text{ref}}^{\text{d}})^4. \quad (27)$$

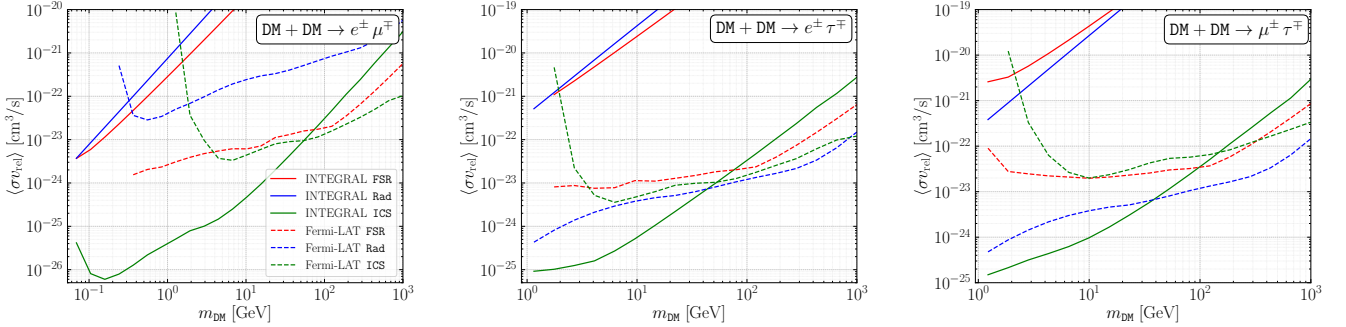


FIG. 5. Comparison of the constraints on $\langle\sigma v_{\text{rel}}\rangle_{ij+ji}$ from the three photon components: FSR (red), Rad (blue), and ICS (green). The constraints are derived from the INTEGRAL (solid) and Fermi-LAT (dashed) datasets.

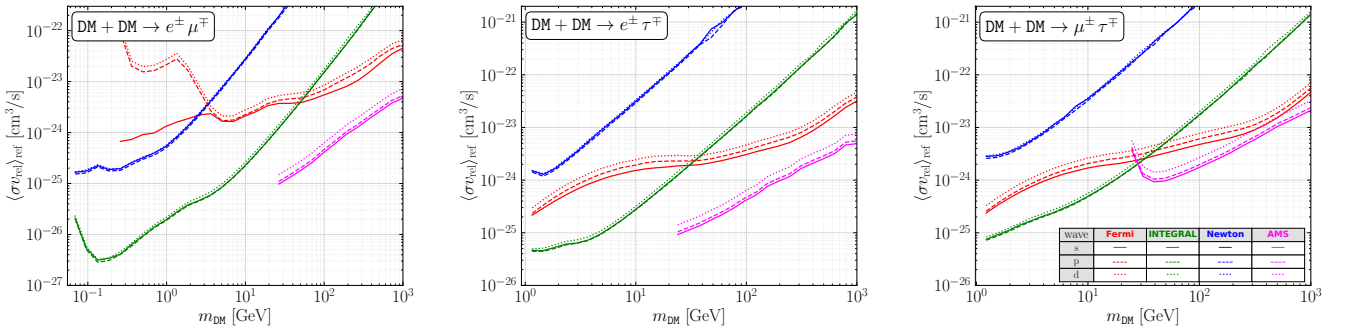


FIG. 6. The 2σ constraints on the annihilation cross sections associated with the s-wave (solid), p-wave (dashed), and d-wave (dotted) contributions from Fermi-LAT (red), INTEGRAL (green), XMM-Newton (blue), and AMS-02(black). To facilitate comparison among different partial waves, a reference annihilation cross section is defined as $\langle\sigma v_{\text{rel}}\rangle_{\text{ref}} \equiv \hat{a}_{2\sigma}, \hat{b}_{2\sigma}(v_{\text{ref}}^{\text{p}})^2$, and $\hat{d}_{2\sigma}(v_{\text{ref}}^{\text{d}})^4$ for the s-, p-, and d-waves, respectively, with $v_{\text{ref}}^{\text{p(d)}} = 1.4(1.7) \times 10^{-3}$.

For INTEGRAL and XMM-Newton, we find that $v_{\text{ref}}^{\text{p}} = 1.4 \cdot 10^{-3}$ and $v_{\text{ref}}^{\text{d}} = 1.7 \cdot 10^{-3}$ for the p- and d-wave cases, respectively. We present the p- and d-wave results in Fig. 6 by rescaling $\hat{b}_{2\sigma}$ and $\hat{d}_{2\sigma}$ by $(v_{\text{ref}}^{\text{p}})^2$ and $(v_{\text{ref}}^{\text{d}})^4$, respectively. From the plots, it can be observed that the required reference velocities for AMS-02 and Fermi-LAT will be slightly smaller. For the $e\mu$ channel shown in the left panel of Fig. 6, the Fermi-LAT constraint deviates from the scaling relation when $m_{\text{DM}} \lesssim 4 \text{ GeV}$. This deviation occurs because the FSR contribution dominates in this mass range, yet only its s-wave contribution is included for the reason discussed in Section III A 1. The constraints are enhanced by a factor of 2 in the real scalar/vector and Majorana fermion DM cases. Notice that the constraints on the s-wave annihilation cross section coincide with the results in our previous work [23].

B. Constraints on EFT operators

In this subsection, we derive the indirect detection constraints on the LFV EFT operators listed in Table I. We discuss the constraints on an effective scale Λ_{eff} associated with each dim- d operator \mathcal{O}_i^d , defined through its corresponding WC C_i^d via the relation $\Lambda_{\text{eff}} \equiv |C_i|^{1/(d-4)}$. Using the leading-order expansions of σv_{rel} induced by the EFT operators given in Table II, the constraints shown in Fig. 6 can be directly translated into bounds on the effective scales associated with the relevant EFT operators, with the exception of $\mathcal{O}_{\ell\chi_2}^{\text{V(A)}}$ and $\mathcal{O}_{\ell\chi_3}^{\text{V(A)}}$. For these two types of operators, the annihilation cross sections receive comparable contributions from two partial waves. Consequently, the constraints on their associated effective scales cannot be inferred from the results in Fig. 6 and must be reevaluated separately using Eq. (26) with $w = \Lambda_{\text{eff}}$. Our results are presented for operators related to the complex scalar/vector and Dirac fermion DM scenarios. In the cases of real scalar/vector and Majorana fermion DM, all operators marked with a ‘X’ in Table I vanish, while for the remaining operators, their effective scales are increased by a factor of $(2\sqrt{2})^{1/(d-4)}$ compared to those of their complex counterparts. Below, we discuss the final constraints for each DM case individually.

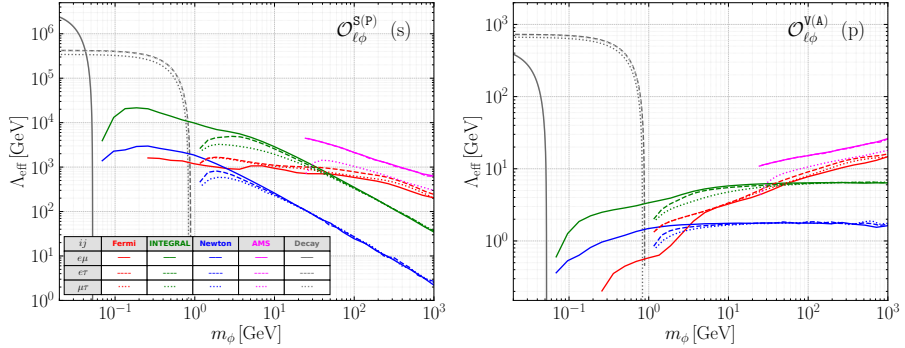


FIG. 7. Constraints on the effective scales associated with dim-5 (left panel) and dim-6 LFV DM-lepton operators in the complex scalar DM case. These constraints are derived from Fermi-LAT (red), INTEGRAL (green), XMM-Newton (blue), and AMS-02 (magenta). The solid, dashed, and dotted curves correspond to the $e\mu$, $e\tau$, and $\mu\tau$ flavor combinations, respectively. The gray curves denote constraints from μ and τ LFV decays into a pair of DM particles, reproduced from [22].

1. Scalar DM case

In Fig. 7, we show the lower bounds on the effective scales for scalar DM operators that involve $e\mu$ (solid), $e\tau$ (dashed), and $\mu\tau$ (dotted) flavor combinations through the three LFV DM annihilation modes. Each pair of operators that differ by a γ_5 in the leptonic current is subject to nearly identical constraints because the mass of the lighter lepton is much smaller than the masses of the DM and heavier lepton partner in each flavor combination. Hence, they are grouped together in the plots throughout the paper. The X/gamma-ray constraints obtained from Fermi-LAT, INTEGRAL, and XMM-Newton are represented by red, green, and blue curves, respectively, while the positron constraints from AMS-02 are depicted in magenta. In addition, we compile existing constraints from charged lepton flavor violating decays $\ell_j \rightarrow \ell_i + \text{DM} + \text{DM}$ [22] as gray curves for comparison.

As can be seen from the two panels, across all operator types, the INTEGRAL telescope provides the most stringent bound in the lower DM mass region ($m_\phi \lesssim 25 \text{ GeV}$), whereas the AMS-02 experiment dominates in the higher mass region ($m_\phi \gtrsim 25 \text{ GeV}$), consistent with the characteristics shown in Fig. 6. In the plots, we also display the dominant partial-wave component in parentheses following the operator label to help understand the constraining features. In the left panel, the dim-5 operators $\mathcal{O}_{\ell\phi}^{S(P)}$ that induce s-wave contributions receive more stringent constraints, with Λ_{eff} reaching $\mathcal{O}(20 \text{ TeV})$ ($\mathcal{O}(6 \text{ TeV})$) for the $e\mu$ ($e\tau$ and $\mu\tau$) flavor case(s), when $m_\phi \approx 0.2$ (3) GeV . The constraints become weaker as the DM mass increases because their σv_{rel} is essentially independent of the DM mass when $m_\phi \gg m_{i,j}$. On the other hand, the dim-6 operators $\mathcal{O}_{\ell\phi}^{V(A)}$ induce p-wave contributions at leading order, resulting in much weaker constraints on their associated Λ_{eff} s, reaching only up to tens of GeV when $m_\phi \gtrsim 200 \text{ GeV}$. The relatively flat behavior observed in the constraints from INTEGRAL and Newton is a joint result of the DM mass enhancement

in their σv_{rel} expansion and the steeply decreasing sensitivity of both telescopes to \hat{b} , as demonstrated in Fig. 6. Although the constraints from charged LFV decays are stronger than the indirect detection by several orders of magnitude, the constraints from DM indirect detection experiments can probe the DM mass range beyond the decay threshold, making those results complementary to each other.

2. Fermion DM case

In Fig. 8, we present the lower bounds on the effective scale of each dim-6 operator in the fermion DM case. Similarly to the scalar DM case, the constraints from DM indirect detection experiments are complementary to those from charged LFV decays. From the third column of Table II, it is clear that, there are 6 operators that contribute dominantly through the s-wave annihilation for the entire kinematically allowed DM mass range: $\mathcal{O}_{\ell\chi 2}^{S(P)}$, $\mathcal{O}_{\ell\chi 1}^{V(A)}$, and $\mathcal{O}_{\ell\chi 1(2)}^T$. For these operators, the constraints on their effective scales are comparable and exhibit similar behavior as the DM mass increases, owing to their analogous quadratic dependence on m_χ when $m_\chi \gg m_{i,j}$. It should be noted that the constraints can reach up to hundreds of GeV when m_χ exceeds the GeV scale. In contrast, the operators $\mathcal{O}_{\ell\chi 1}^{S(P)}$ contribute to the p-wave annihilation in the velocity expansion, resulting in comparably weaker constraints similar to those of the dim-6 operators $\mathcal{O}_{\ell\phi}^{V(A)}$ in the scalar DM case, as shown in Fig. 7.

Finally, for the two operators $\mathcal{O}_{\ell\chi 2}^{V(A)}$, their contribution to σv_{rel} is dominated by the s-wave annihilation up to DM masses around 90 GeV for the $e\mu$ flavor combination and 1.5 TeV for the τ -related flavor combinations, see Fig. 1. Beyond these mass points, the p-wave contribution becomes dominant. Due to these nontrivial features, the corresponding constraints on their associated Λ_{eff} s exhibit significantly different behaviors compared to

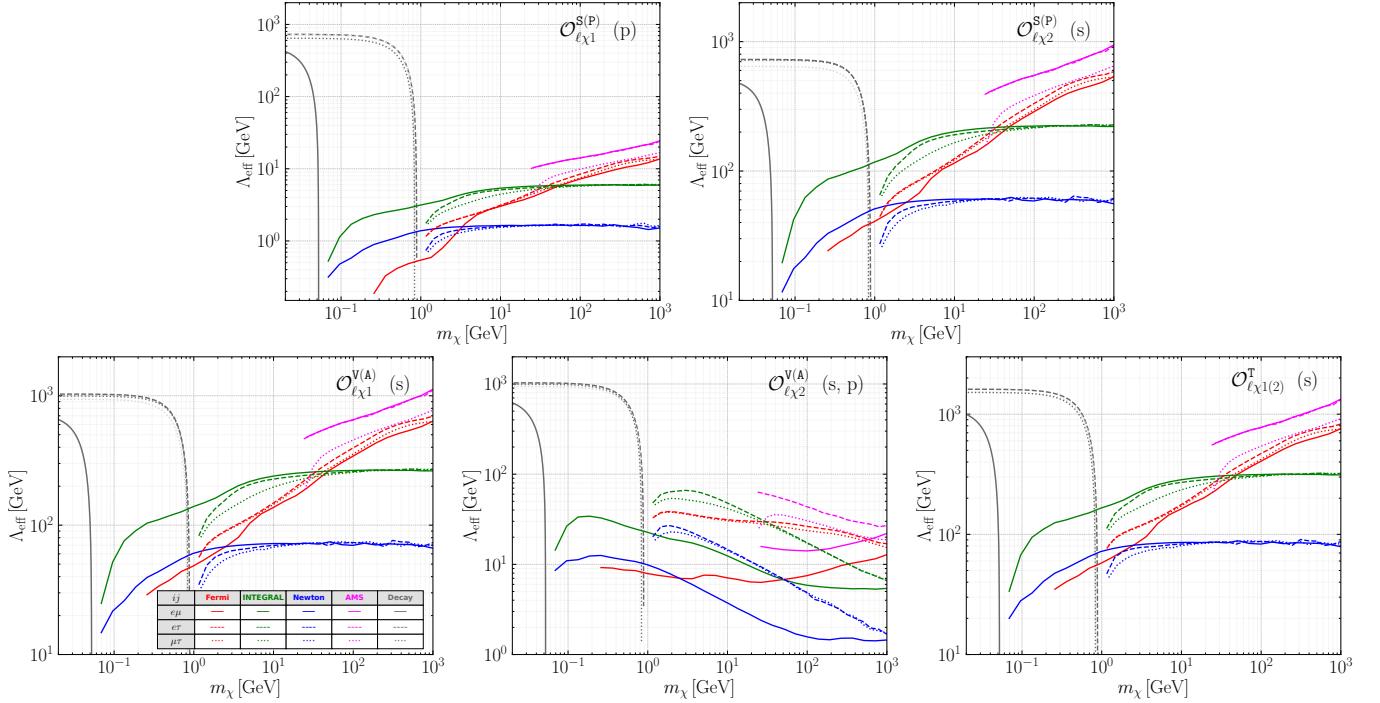


FIG. 8. Same as Fig. 7 but for the Dirac fermion DM case.

operators dominated solely by s- or p-wave contributions. The s-wave component of σv_{rel} is proportional to the mass squared of the heavier final-state lepton through the ratio r_{ij} , as shown in the third column of Table II. Consequently, the $e\tau$ and $\mu\tau$ flavor combinations are subject to more stringent bounds than the $e\mu$ case in all experiments. We find that the INTEGRAL telescope sets the strongest bounds, with values for Λ_{eff} of $e\tau$ flavor combination reaching up to 70 GeV for DM masses around a few GeV.

3. Vector DM case

In the context of charged LFV decays involving light vector DM particles, $\ell_j \rightarrow \ell_i + X + X$, the total decay widths diverge as the DM mass approaches zero, $m_X \rightarrow 0$, in the vector case A, where the operators are formulated in terms of four-vector potentials. To circumvent this issue and set meaningful constraints at smaller values of m_X , Refs. [20, 22] have assumed that each WC in case A is proportional to a minimal power of m_X , which is determined by the number of independent four-vector potentials that cannot be expressed as field strength tensors. We adopt this convention and establish constraints from indirect detection for comparison. Following Ref. [20], we define the effective scale for each operator as follows:

$$C_{\ell X}^{\text{S(P)}} \equiv \frac{m_X^2}{\Lambda_{\text{eff}}^3}, \quad C_{\ell X 1,2}^T \equiv \frac{m_X^2}{\Lambda_{\text{eff}}^3},$$

$$C_{\ell X 1,2,4,5}^{\text{V(A)}} \equiv \frac{m_X^2}{\Lambda_{\text{eff}}^4}, \quad C_{\ell X 3,6}^{\text{V(A)}} \equiv \frac{m_X}{\Lambda_{\text{eff}}^3}. \quad (28)$$

In Fig. 9, we present the constraints on Λ_{eff} s for vector DM case A based on the redefinitions in Eq. (28). Due to the explicit mass factors in the parameterization, the indirect detection constraints on Λ_{eff} s increase as the DM mass rises. Similarly to the scalar and fermion DM scenarios, we incorporate constraints from both astrophysical X/gamma-ray and positron observations, as well as charged LFV decays. From the third column of Table II, it is evident that there are eight operators in case A that contribute predominantly through the s-wave annihilation: $\mathcal{O}_{\ell X}^{\text{S(P)}}$, $\mathcal{O}_{\ell X 1,2}^T$, and $\mathcal{O}_{\ell X 1,6}^{\text{V(A)}}$. Consequently, the constraints on their associated effective scales follow patterns similar to those of the s-wave operators in fermion DM case, with values ranging from a few GeV to TeV, depending on the DM masses. On the other hand, the six operators $\mathcal{O}_{\ell X 2,4,5}^{\text{V(A)}}$ primarily contribute via p-wave annihilation, resulting in constraints that are nearly one order of magnitude weaker than those of s-wave operators at the same DM mass point. For the operators $\mathcal{O}_{\ell X 3}^{\text{V(A)}}$, the contribution is dominated by p-wave annihilation up to DM masses of approximately 90 GeV and 1.5 TeV for the $e\mu$ and τ -related flavor combinations, respectively. Beyond these mass thresholds, the d-wave contribution becomes dominant. Similarly to the operators $\mathcal{O}_{\ell X 2}^{\text{V(A)}}$ in the fermion DM case, the leading p-wave contribution is proportional to the mass squared of the heavier lepton, leading to more stringent bounds on operators involving the $e\tau$ and $\mu\tau$ flavor combinations.

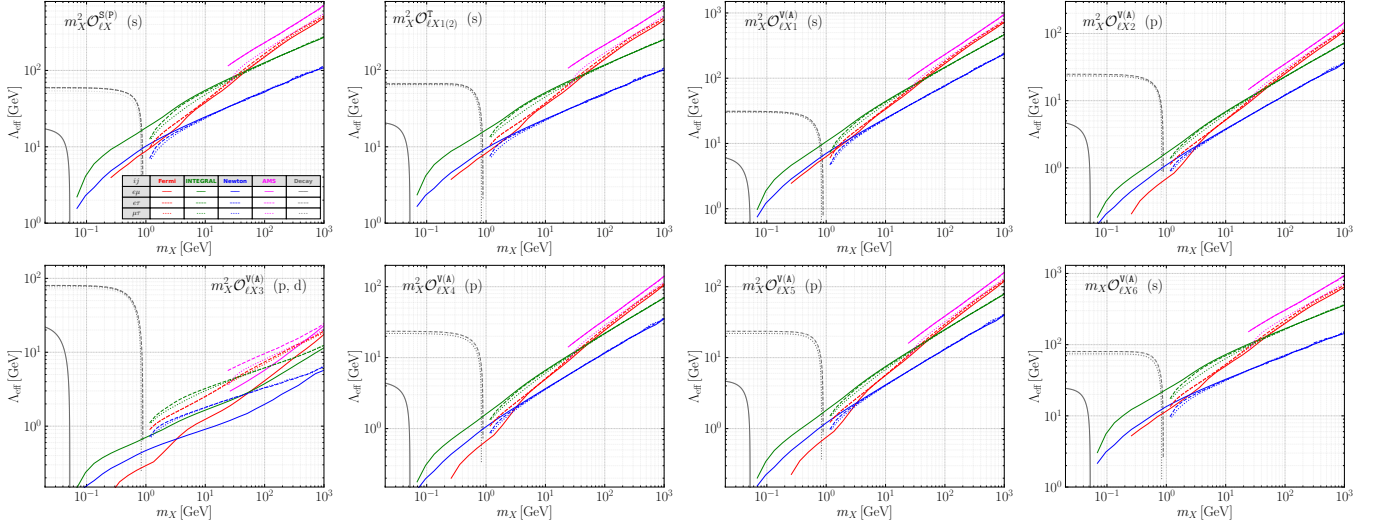


FIG. 9. Same as Fig. 7 but for the complex vector DM case A.

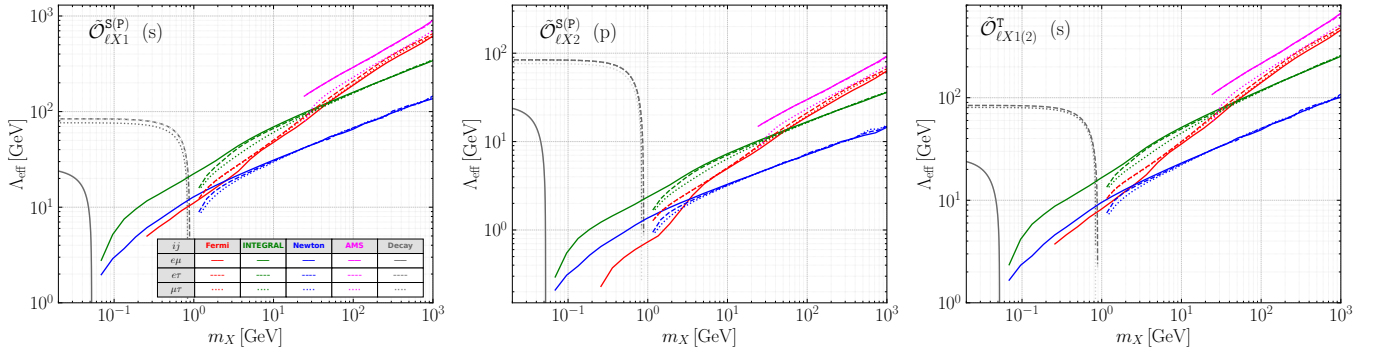


FIG. 10. Same as Fig. 7 but for the complex vector DM case B.

Finally, Fig. 10 presents the results for the vector DM case B, where the operators are parameterized using field strength tensors. The four operators $\tilde{\mathcal{O}}_{\ell X 1}^{S(P)}$ and $\tilde{\mathcal{O}}_{\ell X 1,2}^T$ contribute through s-wave annihilation, while the two operators $\tilde{\mathcal{O}}_{\ell X 2}^{S(P)}$ are dominated by p-wave annihilation. Since these operators are of dimension 7, the constraints on the effective scales of $\tilde{\mathcal{O}}_{\ell X 1}^{S(P)}$ and $\tilde{\mathcal{O}}_{\ell X 1,2}^T$ exhibit similar magnitudes and behavior to those of $m_X^2 \mathcal{O}_{\ell X}^{S(P)}$ in Fig. 9 for the vector case A.

V. SUMMARY

In this study, we systematically explored the constraints on LFV effective interactions between a DM pair and a charged-lepton pair, utilizing the astrophysical photons and positrons observed by Fermi-LAT, INTEGRAL, XMM-Newton, and AMS-02. The DM candidates examined include a scalar, a fermion, and a vector. We collected the leading-order effective operators for each case and derived analytical expressions for the thermally av-

eraged cross-sections induced by these operators. For the photon flux, we considered three main contributions: final-state radiation, radiative decay, and inverse Compton scattering. For FSR, we calculated the photon spectrum for each s-wave operator and found that the normalized spectrum exhibits a mild dependence on the operator structure. In particular, in the observationally relevant energy range, the spectra from all these s-wave operators tend to be degenerate, allowing the FSR spectrum to be approximately described by lepton structure functions when DM mass is much larger than the heavier lepton mass. The comparison of photon flux contributions from these three mechanisms demonstrates that they complement each other in probing different DM mass regions.

For the three LFV annihilation channels, we established meaningful constraints on DM-lepton interactions for different partial wave cases (s, p, d), and found that the resulting limits across different partial waves are related by almost constant velocity-suppression factors. For the three partial wave cases, our results indicate that INTEGRAL provides the most stringent limits for DM masses below 25 GeV or so, while AMS-02

yields the strongest limits for masses above. When we translated these general constraints into effective scales associated with the effective operators, the probed effective scale varies according to the DM candidates, their masses, and the operator structures involved. For dim-5 (dim-6) s-wave operators in the scalar DM scenario, the effective scale can be probed up to 10 TeV (20 GeV). In contrast, for the operators related to fermion and vector DM cases, the probed effective scales can range from GeV to TeV, depending on the DM masses and operator structures. Constraints on p-wave operators are typically weaker by one to two orders of magnitude compared to those on s-wave operators of the same dimension. Interestingly, there are two types of operators, $\mathcal{O}_{\ell\chi^2}^{V(A)}$ and $\mathcal{O}_{\ell\chi^3}^{V(A)}$, which receive significant contributions from two partial waves rather than a single one, with the dominant contribution changing between different DM mass regions. These results complement existing low-energy charged lepton decay constraints when DM mass is below the decay threshold.

In addition to the indirect detection searches examined in this study, these LFV DM scenarios can induce a variety of intriguing signals in different environments. Here, we discuss two possibilities. First, such DM scenarios can inject energy into cosmic fluids during the epoch between recombination and reionization in the early Universe, potentially affecting the anisotropy of the cosmic microwave background [51, 52] and leading to stringent constraints. The second avenue involves collider searches. At lepton colliders, such as Belle II, lepton-flavored DM interactions can be investigated through processes like $e^+ + e^- \rightarrow e^\pm \mu^\mp / e^\pm \tau^\mp / \mu^\pm \tau^\mp$, along with the production of DM particles. However, due to suppression by additional SM couplings and phase space factors, the resulting constraints are expected to be much weaker than those obtained via indirect detection. On the other hand, for the μe flavor case, future facilities such as the Muon collider [53] and the μ TRISTAN proposal [54] have the potential to probe the relevant effective scale up to the TeV level for dim-6 operators, covering a wide range of DM masses and surpassing the indirect bounds established in this work. We postpone these interesting topics in future research.

ACKNOWLEDGMENTS

This work was supported in part by Grants No. NSFC-12305110, No. NSFC-12035008 and No. NSFC-12347112.

Appendix A: Calculation of the general velocity-dependent $\langle\sigma v_{\text{rel}}\rangle$

For DM annihilation into SM particles beyond the s-wave case, the velocity distribution of the initial-state DM particles must be taken into account. The thermally

averaged annihilation cross section is then given by

$$\begin{aligned} \langle\sigma v_{\text{rel}}\rangle(\mathbf{r}) &\equiv \int d^3\mathbf{v}_1 f(\mathbf{r}, \mathbf{v}_1) \int d^3\mathbf{v}_2 f(\mathbf{r}, \mathbf{v}_2) \sigma v_{\text{rel}} \\ &\equiv \int dv_{\text{rel}} F(\mathbf{r}, v_{\text{rel}}) \sigma v_{\text{rel}}. \end{aligned} \quad (\text{A1})$$

Here, \mathbf{v}_1 and \mathbf{v}_2 are the lab-frame velocities of the two initial DM particles, whose velocity distribution is described by $f(\mathbf{r}, \mathbf{v})$ at position \mathbf{r} . Since σv_{rel} depends only on the relative velocity $v_{\text{rel}} = |\mathbf{v}_1 - \mathbf{v}_2|$ in the nonrelativistic limit, it is convenient to first integrate out all other velocity degrees of freedom in the distribution functions and then define a new distribution function $F(\mathbf{r}, v_{\text{rel}})$, as was done in the second step.

In this work, we follow Ref. [29–31] and assume that DM particles obey a three-dimensional Maxwell–Boltzmann velocity distribution with an r -dependent velocity dispersion $v_0(r)$,

$$f(\mathbf{r}, \mathbf{v}) = \frac{1}{(2\pi v_0^2)^{3/2}} \exp\left(-\frac{v^2}{2v_0^2}\right). \quad (\text{A2})$$

Based on the definition in Eq. (A1), it is straightforward to see that

$$F(\mathbf{r}, v_{\text{rel}}) = 4\pi v_{\text{rel}}^2 \frac{1}{(2\pi(2v_0^2))^{3/2}} \exp\left(\frac{-v_{\text{rel}}^2}{2(2v_0^2)}\right). \quad (\text{A3})$$

This shows that the relative-velocity distribution retains the standard Maxwell–Boltzmann form, but with an effective velocity dispersion $\sqrt{2}v_0(r)$. As a result, the moments of the relative velocity are calculated to take the form

$$\begin{aligned} \langle v_{\text{rel}}^{2n} \rangle(\mathbf{r}) &\equiv \int_0^\infty v_{\text{rel}}^{2n} F(\mathbf{r}, v_{\text{rel}}) dv_{\text{rel}} \\ &= 2^n (2n+1)!! v_0^{2n}(r). \end{aligned} \quad (\text{A4})$$

Using the nonrelativistic expansion

$$\sigma v_{\text{rel}} = \hat{a} + \hat{b} v_{\text{rel}}^2 + \hat{d} v_{\text{rel}}^4 + \dots, \quad (\text{A5})$$

the thermally averaged annihilation cross section follows directly as

$$\langle\sigma v_{\text{rel}}\rangle = \hat{a} + 6\hat{b} v_0^2(r) + 60\hat{d} v_0^4(r) + \dots \quad (\text{A6})$$

The velocity dispersion $v_0(r)$ can be obtained by solving the Jeans equation [32, 33]

$$v_0^2(r) = \frac{1}{\rho(r)} \int_\infty^r dr \rho(r) \frac{d\phi}{dr}, \quad (\text{A7})$$

where $\rho(r)$ is the mass density of DM, and $\phi(r)$ is the total gravitational potential at radius r , including contributions from both DM and ordinary matter. Following [31, 55], we model $\phi(r)$ as a sum of three components: the DM halo (ϕ_{halo}), the Milky Way (MW) bulge (ϕ_{bulge}),

and the MW disk (ϕ_{disk}). The DM halo potential with the NFW profile is given by

$$\begin{aligned}\phi(r)_{\text{halo}} &= -G_N \int_0^{r_{\text{vir}}} \frac{\rho(r)}{|r - r'|} d^3 r' \\ &= -4\pi G_N \left[\int_0^r \rho(r') \frac{r'^2}{r} dr' + \int_r^{r_{\text{vir}}} \rho(r') r' dr' \right] \\ &= 4\pi \rho_0 G_N r_s^3 \left\{ \frac{1}{r} \left[\frac{r}{r + r_s} - \log \left(\frac{r + r_s}{r_s} \right) \right] \right. \\ &\quad \left. + \frac{r - r_{\text{vir}}}{(r + r_s)(r_s + r_{\text{vir}})} \right\},\end{aligned}\quad (\text{A8})$$

where G_N is Newton's gravitational constant. The bulge and disk potentials are modeled as [55]

$$\phi(r)_{\text{bulge}} = -\frac{G_N M_b}{r + c_b}, \quad (\text{A9})$$

$$\phi(r)_{\text{disc}} = -\frac{G_N M_d}{r} \left(1 - e^{-r/c_d} \right), \quad (\text{A10})$$

where $M_b = 1.5 \times 10^{10} M_{\odot}$ and $c_b = 0.6$ kpc, while $M_d = 7 \times 10^{10} M_{\odot}$ and $c_d = 4$ kpc, with M_{\odot} denoting the solar mass.

[1] G. Bertone, D. Hooper, and J. Silk, “Particle dark matter: Evidence, candidates and constraints,” *Phys. Rept.* **405** (2005) 279–390 [[hep-ph/0404175](#)].

[2] J. L. Feng, “Dark Matter Candidates from Particle Physics and Methods of Detection,” *Ann. Rev. Astron. Astrophys.* **48** (2010) 495–545 [[arXiv:1003.0904](#)].

[3] L. Roszkowski, E. M. Sessolo, and S. Trojanowski, “WIMP dark matter candidates and searches—current status and future prospects,” *Rept. Prog. Phys.* **81** (2018) 066201 [[arXiv:1707.06277](#)].

[4] G. Arcadi, *et al.*, “The waning of the WIMP? A review of models, searches, and constraints,” *Eur. Phys. J. C* **78** (2018) 203 [[arXiv:1703.07364](#)].

[5] A. Boveia and C. Doglioni, “Dark Matter Searches at Colliders,” *Ann. Rev. Nucl. Part. Sci.* **68** (2018) 429–459 [[arXiv:1810.12238](#)].

[6] M. Schumann, “Direct Detection of WIMP Dark Matter: Concepts and Status,” *J. Phys. G* **46** (2019) 103003 [[arXiv:1903.03026](#)].

[7] A. Arbey and F. Mahmoudi, “Dark matter and the early Universe: a review,” *Prog. Part. Nucl. Phys.* **119** (2021) 103865 [[arXiv:2104.11488](#)].

[8] M. Cirelli, A. Strumia, and J. Zupan, “Dark Matter.” [arXiv:2406.01705](#).

[9] **Belle-II** Collaboration, “Evidence for $B^+ \rightarrow K^+ \nu \bar{\nu}$ decays,” *Phys. Rev. D* **109** (2024) 112006 [[arXiv:2311.14647](#)].

[10] X.-G. He, X.-D. Ma, and G. Valencia, “Revisiting models that enhance $B^+ \rightarrow K^+ \nu \bar{\nu}$ in light of the new Belle II measurement,” *Phys. Rev. D* **109** (2024) 075019 [[arXiv:2309.12741](#)].

[11] X.-G. He, X.-D. Ma, M. A. Schmidt, G. Valencia, and R. R. Volkas, “Scalar dark matter explanation of the excess in the Belle II $B^+ \rightarrow K^+ + \text{invisible}$ measurement,” *JHEP* **07** (2024) 168 [[arXiv:2403.12485](#)].

[12] A. Berezhnoy and D. Melikhov, “ $B \rightarrow K^* M_X$ vs $B \rightarrow K M_X$ as a probe of a scalar-mediator dark matter scenario,” *EPL* **145** (2024) 14001 [[arXiv:2309.17191](#)].

[13] L. Calibbi, T. Li, L. Mukherjee, and M. A. Schmidt, “Is dark matter the origin of the $B \rightarrow K \nu \bar{\nu}$ excess at Belle II?” *Phys. Rev. D* **112** (2025) 075020 [[arXiv:2502.04900](#)].

[14] K. Ding, *et al.*, “Resonant ALP-Portal Dark Matter Annihilation as a Solution to the $B^{\pm} \rightarrow K^{\pm} \nu \bar{\nu}$ Excess.” [arXiv:2504.00383](#).

[15] Z.-K. Liu, Y. Li, B.-F. Hou, and Q. Chang, “Search for Light Dark Matter in Rare Meson Decays.” [arXiv:2512.21191](#).

[16] Z.-j. Tao, “Radiative seesaw mechanism at weak scale,” *Phys. Rev. D* **54** (1996) 5693–5697 [[hep-ph/9603309](#)].

[17] E. Ma, “Verifiable radiative seesaw mechanism of neutrino mass and dark matter,” *Phys. Rev. D* **73** (2006) 077301 [[hep-ph/0601225](#)].

[18] H. Acaroglu, P. Agrawal, and M. Blanke, “Lepton-flavoured scalar dark matter in Dark Minimal Flavour Violation,” *JHEP* **05** (2023) 106 [[arXiv:2211.03809](#)].

[19] H. Davoudiasl, J. Hoefken Zink, and S. Trojanowski, “Flavor blocking of dark matter thermalization in neutron stars.” [arXiv:2511.05651](#).

[20] X.-G. He, X.-D. Ma, and G. Valencia, “FCNC B and K meson decays with light bosonic Dark Matter,” *JHEP* **03** (2023) 037 [[arXiv:2209.05223](#)].

[21] J.-H. Liang, Y. Liao, X.-D. Ma, and H.-L. Wang, “Dark sector effective field theory,” *JHEP* **12** (2023) 172 [[arXiv:2309.12166](#)].

[22] S. Jahedi, Y. Liao, and X.-D. Ma, “Charged lepton flavor violating decays with a pair of light dark matter and muonium invisible decay.” [arXiv:2507.13876](#).

[23] J.-H. Liang, Y. Liao, and X.-D. Ma, “Probing lepton flavor violating dark matter scenarios via astrophysical photons and positrons.” [arXiv:2508.05121](#).

[24] **Fermi-LAT** Collaboration, “Fermi-LAT Observations of the Diffuse Gamma-Ray Emission: Implications for Cosmic Rays and the Interstellar Medium,” *Astrophys. J.* **750** (2012) 3 [[arXiv:1202.4039](#)].

[25] L. Bouchet, *et al.*, “Diffuse emission measurement with INTEGRAL/SPI as indirect probe of cosmic-ray electrons and positrons,” *Astrophys. J.* **739** (2011) 29 [[arXiv:1107.0200](#)].

[26] J. W. Foster, *et al.*, “Deep Search for Decaying Dark Matter with XMM-Newton Blank-Sky Observations,” *Phys. Rev. Lett.* **127** (2021) 051101 [[arXiv:2102.02207](#)].

[27] **AMS** Collaboration, “Towards Understanding the Origin of Cosmic-Ray Positrons,” *Phys. Rev. Lett.* **122** (2019) 041102.

[28] V. Shtabovenko, R. Mertig, and F. Orellana, “New Developments in FeynCalc 9.0,” *Comput. Phys. Commun.* **207** (2016) 432–444 [[arXiv:1601.01167](#)].

[29] B. Robertson and A. Zentner, “Dark Matter Annihilation Rates with Velocity-Dependent Annihilation Cross Sections,” *Phys. Rev. D* **79** (2009)

083525 [[arXiv:0902.0362](https://arxiv.org/abs/0902.0362)].

[30] Y. Zhao, X.-J. Bi, H.-Y. Jia, P.-F. Yin, and F.-R. Zhu, “Constraint on the velocity dependent dark matter annihilation cross section from Fermi-LAT observations of dwarf galaxies,” *Phys. Rev. D* **93** (2016) 083513 [[arXiv:1601.02181](https://arxiv.org/abs/1601.02181)].

[31] C. A. Argüelles, *et al.*, “Dark matter annihilation to neutrinos,” *Rev. Mod. Phys.* **93** (2021) 035007 [[arXiv:1912.09486](https://arxiv.org/abs/1912.09486)].

[32] J. Binney and S. Tremaine, *Galactic dynamics*. Princeton university press, 2011.

[33] F. Ferrer and D. R. Hunter, “The impact of the phase-space density on the indirect detection of dark matter,” *JCAP* **09** (2013) 005 [[arXiv:1306.6586](https://arxiv.org/abs/1306.6586)].

[34] J. F. Navarro, C. S. Frenk, and S. D. M. White, “The Structure of cold dark matter halos,” *Astrophys. J.* **462** (1996) 563–575 [[astro-ph/9508025](https://arxiv.org/abs/astro-ph/9508025)].

[35] J. F. Navarro, C. S. Frenk, and S. D. M. White, “A Universal density profile from hierarchical clustering,” *Astrophys. J.* **490** (1997) 493–508 [[astro-ph/9611107](https://arxiv.org/abs/astro-ph/9611107)].

[36] M. Cirelli, *et al.*, “PPPC 4 DM ID: A Poor Particle Physicist Cookbook for Dark Matter Indirect Detection,” *JCAP* **03** (2011) 051 [[arXiv:1012.4515](https://arxiv.org/abs/1012.4515)]. [Erratum: *JCAP* 10, E01 (2012)].

[37] T. Lin, “Dark matter models and direct detection,” *PoS* **333** (2019) 009 [[arXiv:1904.07915](https://arxiv.org/abs/1904.07915)].

[38] O. Nicrosini and L. Trentadue, “SECOND ORDER ELECTROMAGNETIC RADIATIVE CORRECTIONS TO $e^+ e^- \rightarrow \gamma\gamma^*$, $Z0 \rightarrow \mu^+ \mu^-$,” *Z. Phys. C* **39** (1988) 479.

[39] Y. Kuno and Y. Okada, “Muon decay and physics beyond the standard model,” *Rev. Mod. Phys.* **73** (2001) 151–202 [[hep-ph/9909265](https://arxiv.org/abs/hep-ph/9909265)].

[40] C. Bierlich *et al.*, “A comprehensive guide to the physics and usage of PYTHIA 8.3,” *SciPost Phys. Codeb.* **2022** (2022) 8 [[arXiv:2203.11601](https://arxiv.org/abs/2203.11601)].

[41] M. Regis and P. Ullio, “Multi-wavelength signals of dark matter annihilations at the Galactic center,” *Phys. Rev. D* **78** (2008) 043505 [[arXiv:0802.0234](https://arxiv.org/abs/0802.0234)].

[42] M. Cirelli and P. Panci, “Inverse Compton constraints on the Dark Matter e^+e^- excesses,” *Nucl. Phys. B* **821** (2009) 399–416 [[arXiv:0904.3830](https://arxiv.org/abs/0904.3830)].

[43] M. Cirelli, N. Fornengo, B. J. Kavanagh, and E. Pinetti, “Integral X-ray constraints on sub-GeV Dark Matter,” *Phys. Rev. D* **103** (2021) 063022 [[arXiv:2007.11493](https://arxiv.org/abs/2007.11493)].

[44] P. Meade, M. Papucci, A. Strumia, and T. Volansky, “Dark Matter Interpretations of the e^+e^- Excesses after FERMI,” *Nucl. Phys. B* **831** (2010) 178–203 [[arXiv:0905.0480](https://arxiv.org/abs/0905.0480)].

[45] I. Cholis, G. Dobler, D. P. Finkbeiner, L. Goodenough, and N. Weiner, “The Case for a 700+ GeV WIMP: Cosmic Ray Spectra from ATIC and PAMELA,” *Phys. Rev. D* **80** (2009) 123518 [[arXiv:0811.3641](https://arxiv.org/abs/0811.3641)].

[46] E. Borriello, A. Cuoco, and G. Miele, “Secondary radiation from the Pamela/ATIC excess and relevance for Fermi,” *Astrophys. J. Lett.* **699** (2009) L59–L63 [[arXiv:0903.1852](https://arxiv.org/abs/0903.1852)].

[47] G. R. Blumenthal and R. J. Gould, “Bremsstrahlung, synchrotron radiation, and compton scattering of high-energy electrons traversing dilute gases,” *Rev. Mod. Phys.* **42** (1970) 237–270.

[48] A. E. Vladimirov, *et al.*, “GALPROP WebRun: an internet-based service for calculating galactic cosmic ray propagation and associated photon emissions,” *Comput. Phys. Commun.* **182** (2011) 1156–1161 [[arXiv:1008.3642](https://arxiv.org/abs/1008.3642)].

[49] https://github.com/bsafdi/XMM_BSO_DATA.

[50] M. Cirelli, N. Fornengo, J. Koechler, E. Pinetti, and B. M. Roach, “Putting all the X in one basket: Updated X-ray constraints on sub-GeV Dark Matter,” *JCAP* **07** (2023) 026 [[arXiv:2303.08854](https://arxiv.org/abs/2303.08854)].

[51] T. R. Slatyer, “Indirect dark matter signatures in the cosmic dark ages. I. Generalizing the bound on s-wave dark matter annihilation from Planck results,” *Phys. Rev. D* **93** (2016) 023527 [[arXiv:1506.03811](https://arxiv.org/abs/1506.03811)].

[52] T. R. Slatyer and C.-L. Wu, “General Constraints on Dark Matter Decay from the Cosmic Microwave Background,” *Phys. Rev. D* **95** (2017) 023010 [[arXiv:1610.06933](https://arxiv.org/abs/1610.06933)].

[53] International Muon Collider Collaboration, “The Muon Collider,” [arXiv:2504.21417](https://arxiv.org/abs/2504.21417).

[54] Y. Hamada, R. Kitano, R. Matsudo, H. Takaura, and M. Yoshida, “ μ TRISTAN,” *PTEP* **2022** (2022) 053B02 [[arXiv:2201.06664](https://arxiv.org/abs/2201.06664)].

[55] K. K. Boddy, J. Kumar, and L. E. Strigari, “Effective J -factor of the Galactic Center for velocity-dependent dark matter annihilation,” *Phys. Rev. D* **98** (2018) 063012 [[arXiv:1805.08379](https://arxiv.org/abs/1805.08379)].